

Jetted Subgalactic-Size Radio Sources in Merging Galaxies

A Jet Redirection Scenario

C. Stanghellini¹, M. Orienti¹, C. Spingola¹, A. Zanichelli¹, D. Dallacasa^{1,2}, P. Cassaro³, C. P. O’Dea⁴, S. A. Baum⁴,
and M. Pérez-Torres^{5,6}

¹ INAF – Istituto di Radioastronomia, via Gobetti 101, I-40129 Bologna, Italy
e-mail: carlo.stanghellini@inaf.it

² Dipartimento di Fisica e Astronomia, Università di Bologna, via Gobetti 93/2, I-40129 Bologna, Italy

³ INAF – Istituto di Radioastronomia, Stazione di Noto, Contrada Renna Bassa, I-96017 Noto, Italy

⁴ Department of Physics & Astronomy, University of Manitoba, 30A Sifton Rd., Winnipeg, MB R3T 2N2, Canada

⁵ Consejo Superior de Investigaciones Científicas (CSIC) - Instituto de Astrofísica de Andalucía (IAA), Glorieta de la Astronomía s/n, 18008 Granada, Spain

⁶ School of Sciences, European University Cyprus, Diogenes street, Engomi, 1516 Nicosia, Cyprus

July 3, 2024

ABSTRACT

Context. The long-standing question concerning Jetted Sub-Galactic Size (JSS) radio sources is whether they will evolve into large radio galaxies, die before escaping the host galaxy, or remain indefinitely confined to their compact size.

Aims. Our main goal is to propose a scenario that explains the relative number of JSS radio sources and their general properties.

Methods. We studied the parsec-scale radio morphology of a complete sample of 21 objects using Very Long Baseline Interferometry (VLBI) observations at various frequencies and analyzed the morphological characteristics of their optical hosts.

Results. Many of these radio sources exhibit radio morphologies consistent with transverse motions of their bright edges and are located in dynamically disturbed galaxies. VLBI images provide evidence for large-angle, short-period precessing jets, and the orbital motion of the radio-loud AGN in a dual or binary system. The majority of JSS radio sources are in systems in different stages of their merging evolution.

Conclusions. We propose a scenario where the rapid jet redirection, through precession or orbital motion, prevents the jet from penetrating the interstellar medium (ISM) sufficiently to escape the host galaxy. Most JSS radio sources remain compact due to their occurrence in merging galaxies.

Key words. Galaxies: active – Galaxies: jets – Galaxies: interactions – Radio continuum: galaxies – Techniques: high angular resolution – Techniques: interferometric

1. Introduction

A significant fraction of extragalactic radio sources (10-30%, depending on flux density limit and observing frequency of the radio surveys) are intrinsically compact, with projected sizes smaller than their host galaxy. The simplest scenario to explain their compactness is to propose that they represent the initial phase of the radio AGN phenomenon and will eventually evolve into classical Fanaroff-Riley (FR) radio sources. However, if we assume that radio sources grow at a uniform speed, their number is too large to support the "youth scenario" unless we invoke a strong luminosity evolution (Fanti et al. 1995; O’Dea & Baum 1997). The alternative "frustration scenario" suggests that these radio sources are confined by a dense interstellar medium (ISM) for an extended time, or even indefinitely, within the inner regions of the host galaxy (van Breugel et al. 1984). However, the existence of such a dense environment has remained elusive (Fanti et al. 2000; Siemiginowska et al. 2005; Vink et al. 2006). Even when an interaction between jets and the ISM is observed, the amount of gas present appears insufficient to confine the radio source indefinitely (Morganti et al. 2004; Labiano et al. 2005, 2006; Morganti et al. 2013; Schulz et al. 2021). The "short lived" scenario is another alternative, considering that most of these

AGNs will turn off the radio activity in a few thousand years, a time too short to expand outside the host galaxy (Readhead et al. 1994, 2023; Reynolds & Begelman 1997; Czerny et al. 2009; Orienti & Dallacasa 2020; Kiehlmann et al. 2024b). In particular, it has been suggested that the majority of Compact Symmetric Objects (CSOs) are transient objects formed by a tidal disruption event (TDE) of giant stars. These events involve an energy budget sufficient to turn on the radio source only for a very short time (Kiehlmann et al. 2024a,b; Readhead et al. 2024; Sullivan et al. 2024).

Given their intrinsically small sizes, the emitting region undergoes synchrotron self-absorption (SSA), generating a distinctive peak in the radio spectrum, which provides an effective tool for their selection (Gopal-Krishna et al. 1983; O’Dea 1998; Snellen et al. 2000). Alternatively, the spectral peak may be caused by free-free absorption (FFA) from ionized gas in front of the emitting region (e.g. Bicknell et al. 1997; Tingay et al. 2015). A combination of both effects may be present in some objects (e.g. Orienti & Dallacasa 2008). Historically, different names and acronyms have been used depending on where the radio peak was searched: Compact Steep Spectrum (CSS) radio sources have been selected from low-frequency surveys as having a steep radio spectrum and a size smaller than 20 kpc

(Fanti et al. 1990, 1995). GHz-Peaked-Spectrum (GPS) radio sources are selected based on their convex radio spectrum peaking around 1 GHz, and, as a consequence, generally have sizes not exceeding ~ 1 kpc (O’Dea et al. 1991; Stanghellini et al. 1998). High Frequency Peakers (HFP) extend the GPS class to radio sources peaking around or above 5 GHz, with even smaller sizes (Dallacasa et al. 2000; Stanghellini et al. 2009a). GPS radio sources and HFPs are included in the class of Peaked Sources (PS) in the extended review by O’Dea & Saikia 2021. CSOs with a linear size (LS) < 1 kpc, and middle-sized symmetric objects (MSOs) with $1 \text{ kpc} < \text{LS} < 20 \text{ kpc}$ are the same class of radio sources as CSS and GPS, but selected according to their radio structure rather than spectral properties (Wilkinson et al. 1994; Readhead et al. 1996a,b). Each of these selection criteria has its own drawbacks. Selection based on the spectral properties can include contaminating objects with similar spectral appearance but of different nature (e.g. blazars). Conversely, CSOs might exclude objects that, for various reasons, lack evident symmetry but are still part of the same class of jetted radio sources embedded within the host galaxy.

To define a homogeneous class that includes all the above categories based on the intrinsic property of interest, we introduce the class of Jetted Subgalactic Size (JSS) radio sources, meaning radio-loud AGNs with an intrinsic size of the radio emission that does not extend outside the host galaxy. Therefore, the class of Jetted Subgalactic Size radio sources includes all the CSOs and the CSS/PS sources, excluding contaminating blazars.

These powerful radio sources may have jets, lobes, hot spots, and cores, similar to large FR radio galaxies, but on a smaller scale. Not all of these components are necessarily visible, and central cores, in particular, appear rather elusive. The morphology is often irregular, and the two sides of the radio source differ significantly in size and brightness (Saikia et al. 2003; Rossetti et al. 2008; Dallacasa et al. 2013; Morganti & Oosterloo 2018). These sources are weakly polarized, with fractional polarization increasing, and Rotation Measure (RM) decreasing with size (Stanghellini et al. 1998, 2001; Cotton et al. 2003; Fanti et al. 2004; Rossetti et al. 2008). The irregular morphology and depolarization suggest that the radio source is embedded in a dense, ionized, and inhomogeneous environment, which becomes clumpier towards the center of the galaxy.

Sometimes faint and diffuse emission is seen on the arcsecond scale (Baum et al. 1990; Marecki et al. 2003; Stanghellini et al. 2005), which is interpreted as relic emission from past radio activity of the AGN. The optical hosts of JSS radio sources are generally galaxies, whereas the great majority of quasars found in samples of PS sources are contaminating objects that appear bright and compact due to beaming and projection effects (Stanghellini 2003).

JSS radio sources have been detected in X-rays only with the advent of sensitive X-ray telescopes. It is not clear whether the X-ray emission is of thermal origin, attributed to hot shocked gas or gas falling into the accretion disk, or of nonthermal origin (synchrotron or inverse Compton scattering) coming from the base of the jet (Ostorero et al. 2010; O’Dea et al. 2017; Sobolewska et al. 2019). Recent works, including γ -ray studies, suggest the presence of high-energy emission of nonthermal origin, possibly associated with the jet and/or lobes (Principe et al. 2021; Sobolewska et al. 2023; Bronzini et al. 2024).

In this work, we present a radio morphological study at parsec scale for a complete sample of JSS radio sources, with additional considerations on the morphological aspect of their optical hosts. We also present a novel scenario to explain the com-

pactness and the count excess of Jetted Subgalactic Size radio sources.

Throughout this paper, we assume the following cosmology: $H_0 = 70 \text{ km s}^{-1} \text{ Mpc}^{-1}$, $\Omega_M = 0.27$, and $\Omega_\Lambda = 0.73$, in a flat Universe. The spectral index α is defined as $S(\nu) \propto \nu^{-\alpha}$.

2. The sample

Many samples of JSS radio sources have been constructed from various radio surveys, as listed in O’Dea & Saikia (2021). In this paper, we focus on the 1 Jy complete sample of GPS radio sources selected by Stanghellini et al. (1998), to construct a complete sample of JSS radio sources. These sources are compact, powerful, and bright enough to allow for detailed study at parsec scales using Very Long Baseline Interferometry (VLBI) techniques. In subsequent papers, we will expand the size range to include both larger and smaller scales, incorporating sources selected from current samples of CSS and HFP radio sources.

It has been found that samples selected based solely on spectral properties contain a significant fraction of blazars, which contaminate the sample of genuine compact sources, showing core-jet morphology and/or significant radio variability. (Stanghellini 2003; Tornaiainen et al. 2005; Orienti et al. 2007, 2010a; Orienti & Dallacasa 2008). While it is true that some genuine compact sources may have the jet aligned with the line of sight, their spectra should generally be flat. The convex spectral shape seen in blazars is likely produced by a dominant distinct component in a relativistic beamed jet. Although these blazars are interesting objects on their own, they represent a separated population of objects compared to genuine compact radio galaxies.

Therefore, we refined the original 1 Jy sample, retaining only the objects that present emission on both sides of a putative center of activity, which may be undetected due to sensitivity limitations or visible as a flat-spectrum compact component.

The final complete sample of genuine Jetted Subgalactic Size radio sources consists of 21 radio sources with a flux density $S > 1$ Jy at 5 GHz, declination $\delta > -25^\circ$, galactic latitude $|b| > 20^\circ$, and a radio spectrum peaking between 0.4 and 6 GHz (Table 1). These are identified with galaxies, with a few exceptions.

3. The data

3.1. VLBI observations and archival data

A turnover frequency around 1 GHz preferentially selects radio sources with angular sizes from a few mas to a few hundred mas, making VLBI observations the best way to study their morphology in detail.

We performed VLBA observations of 14 out of the 21 JSS sources in the sample (projects BS085 on 27 Mar, 30 Apr, 13 May, 9 Jun 2001, and BO030 on 23 Mar, 27 Apr 2008). To complete the morphological study for the entire sample, we complemented our observations with reprocessed archival data for the remaining sources.

Observations from projects BS085 and BO030 are highlighted in boldface in Table 1. While many objects already have VLBI information available in the literature, we chose to present images for all objects in our complete sample because, in most cases, our reprocessed data reveal additional important details. In a few cases, we concatenated data from different projects to improve the UV-coverage, as variability in flux density and structure is negligible. In Table 2 we list the archival VLBA data considered in this work.

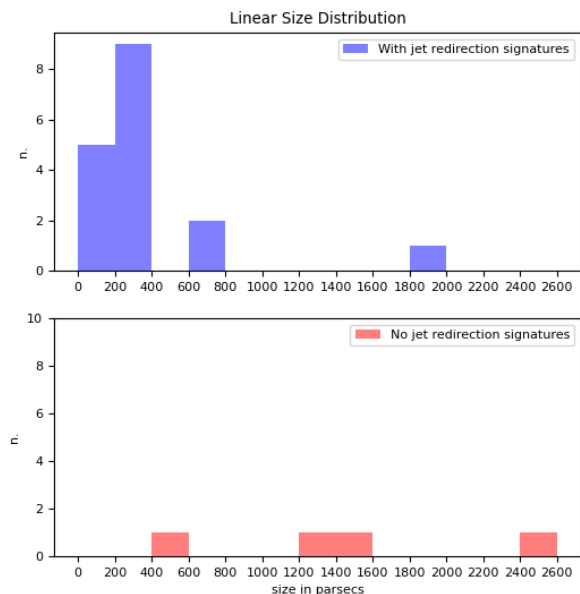


Fig. 1. Projected linear size distribution for radio sources with (top) or without (bottom) indication of jet redirection

Calibration of the VLBI data has been carried out using the Astronomical Image Processing System (AIPS, Greisen 1990) following standard procedures. The calibrated visibilities were then exported to the DIFMAP software package (Shepherd 1997) for self-calibration and imaging. The resulting FITS files of the final images were imported back into AIPS for data analysis and to produce the final figures shown in Figs. 4 to 24.

The uv-coverage and sensitivity of the images did not allow for reliable spectral index maps. Therefore, we calculated the spectral index only for compact components or integrating over isolated extended components (Table 3). Even so, high frequency images were unable to properly recover the whole flux density for extended structures, leading to an artificial steepening of the spectrum. These images may only be used to identify flat components that we can possibly associate with a radio core. Flux density errors of the listed components are dominated by calibration uncertainties and can be conservatively considered as 10%, without taking into account the missing flux density for unsampled spatial frequencies.

3.2. Optical images

We collected images of the optical hosts of our radio sources to review their optical morphology and intergalactic environment. We selected the best images available from various sources, including the Sloan Digital Sky Survey (SDSS; Abdurro'uf et al. 2022), the Pan-STARRS survey (Chambers et al. 2016), and reprocessed images from those observed by Stanghellini et al. (1993). When stacking images from different filters resulted in improved detail, we utilized those composite images. The optical images, along with the corresponding radio band images, are presented in Figs. 4 to 24.

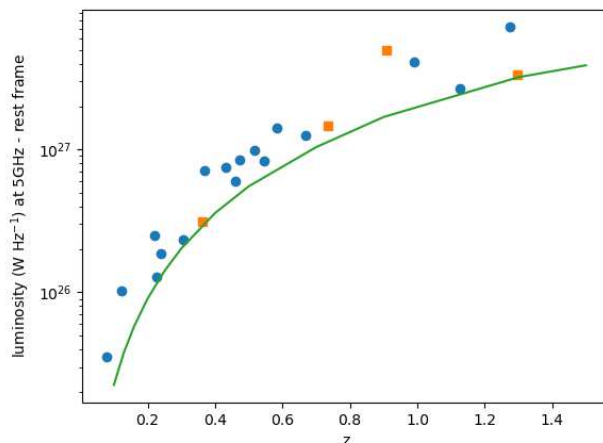


Fig. 2. Luminosity at 5GHz rest frame. Circles are objects with jet redirection signatures, squares are object with no jet redirection signatures

4. Results

4.1. Recurrent patterns in radio morphology

The JSS radio sources studied in this work exhibit a variety of morphologies. While each object has its unique characteristics, which we will detail in the notes on individual objects, we recognize several distinctive features. Following the approach in Krause et al. (2019), we look for signatures that indicate the possible presence of a precessing radio jet and/or, in our case, the possible or likely occurrence of an orbital motion of the radio AGN. We consider five morphological markers in the radio and one in the optical (the first two in common with Krause et al. (2019)).

(C) - Presence of a curved jet.

(S) - An overall appearance characterized by an S-shaped morphology.

(T) - Presence of a transverse lobe, i.e. significant low-brightness emission extending from the hot spot to one side relative to the radio source axis. When there is clear evidence that this emission extends in opposite directions with respect to the radio source axis (displaying radial symmetry), we denote this as T_O . Conversely, when the emission extends from the hot spot in the same direction with respect to the radio source axis (displaying axial symmetry) we denote it as T_S .

(A) - Presence of an arc-like component in the emission around the hot spot or extending from it.

(L) - A ratio <2 between the length and the "width" of the radio source, based on the image with the highest sensitivity to extended emission. The length is the distance between the hot spots when these are present, or the maximum extension of radio emission, while the width is the maximum extension of the radio emission perpendicular to the source axis.

(D) - Disturbed morphology of the host galaxy. When the optical host is faint, but still shows hints of an irregular shape or disturbed morphology, we denote it as d (lower case).

Last columns in Table 1 indicate the presence of these morphological markers in each object, with 17 objects showing two or more of these signatures and 4 objects showing none.

Table 1. The sample. Columns are: source name (projects BS085 and BO030 in bold), source name in J2000 coordinates, alternative name, optical identification, optical magnitude, redshift, scale, size, luminosity at 5 GHz, precession/orbital markers from radio images, and merger marker from optical images (see Sect. 4.1).

Source	J2000	alt. name	id	m	z	scale (pc/mas)	size (pc)	$L_{5\text{GHz}}$ (10^{26}W/Hz)	prec./orb. markers	merger marker
0019-000	J0022+0014	4C+00.02	G	18.4r	0.306	4.55	360	2.2	CT _O	D
0108+388	J0111+3906		G	22.0r	0.669	7.22	45	11	ST	
0316+162	J0318+1628	CTA21	G	23.6r	0.907	7.92	2400	41		
0428+205	J0431+2037	DA138	G	19.3r	0.219	3.57	790	2.4	LAT	D
0500+019	J0503+0223		G	21.0i	0.585	6.77	95	12	S	d
0710+439	J0713+4349		G	20.4r	0.518	6.42	190	8.7	AT _O	D
0941-080	J0943+0819		G	17.9r	0.228	3.79	340	1.2	AT _O	D
1031+567	J1035+5628		G	20.2r	0.459	6.01	180	5.3	LT _O	D
1117+146	J1120+1420	4C+14.41	G	20.1R	0.363	5.21	520	2.9		
1245-197	J1248-1959		Q	20.5V	1.275	8.49	1900	56	AT _O	d
1323+321	J1326+3154	4C+32.44	G	19.2r	0.369	5.27	320	6.6	LAT	D
1345+125	J1347+1217	4C+12.50	G	15.5r	0.122	2.23	220	0.98	S	D
1358+624	J1400+6210	4C+62.22	G	19.8r	0.429	5.78	290	6.7	LAT _O	D
1404+286	J1407+2827	OQ208,MRK668	G	14.6r	0.077	1.47	12	0.35	T _S	D
1518+047	J1521+0430	4C+04.51	G	22.6r	1.296	8.60	1400	26		
1607+268	J1609+2641	CTD93	G	20.4r	0.473	6.08	330	7.6	T _O	d
2008-068	J2011-0644		G	20.9i	0.547	7.55	230	7.3	T _S	d
2128+048	J2130+0502		G	23.3r	0.99	8.21	290	33	CT _S	d
2210+016	J2212+0152	4C+01.69	G	21.7r	1.126	7.27	650	20	LCT	
2342+821	J2344+8226		Q	20.1r	0.735	7.51	1350	12		
2352+495	J2355+4950		G	18.4R	0.238	3.91	195	1.8	LSAT _O	D

4.2. Notes on individual sources

In the following, we provide for each object the relevant information from the literature and a description of our findings. Unless otherwise indicated, the basic information reported is drawn from the NASA/IPAC Extragalactic Database (NED)¹.

0019-000: This is a 18.4r magnitude galaxy at $z=0.306$. There is little information in the literature on the parsec-scale morphology of this source. Fey et al. (2002) present images at 2.3 and 8.7 GHz, showing a structure resembling a core-jet morphology. However, our VLBA images at the L,C,X bands reveal a more complex morphology. The northern component is extended and has a steep spectrum, indicating it is unlikely to be the core. We identify the two brightest components at the edges of the radio structure as the hot spots. A curved, interrupted trail of emission connects these brighter components, and further emission extends transversely to the jet axis at L band. The most likely explanation is that projection effects distort a double morphology. There is no evidence of a compact and flat spectrum component that could be identified as the core. The optical host appears as a double-interacting galaxy with a few much weaker objects within a distance of 20 arcseconds.

0108+388: The optical host is a 22.0r magnitude galaxy at $z=0.669$. A similar weak object is present at a distance of 20 arcseconds. Notably, the arcsecond-scale radio emission, previously detected near the compact radio source (Baum et al. 1990), coincides with this optical object, challenging its direct association with the compact radio source. Other unresolved and bright objects in the optical field are likely foreground stars. The radio morphology comprises two curved and knotty jets terminating in two hotspots. At 5 and 8.3 GHz, extended emission widening

towards the northwest is detected. Taylor et al. (1996) identify an inverted spectrum component at the center of the radio emission as the core. However, this component is not clearly distinguishable in our images, possibly due to variability. Polatidis & Conway (2003) report a separation speed of $0.26c$ between the two hot spots.

0316+162: The optical host is a faint galaxy (23.6 r magnitude at $z=0.907$), surrounded by other objects within a 10 arcsecond distance. The radio morphology exhibits an asymmetric double radio source, characterized by high flux density and arm-length ratios between the two sides. The images reveal a faint, rather amorphous southern part, while the northern part resembles a jet termination. Dallacasa et al. (2021) present a global VLBI image at 327 MHz, which is consistent with our 609 MHz image. Dallacasa et al. (2013) identified the component Ce3 in our images as the core. However, Frey & Titov (2021) revised this identification, suggesting that Ce1 component we detect at 5 GHz but not at lower frequencies, might be the core. The lack of detection below 5 GHz in our images indicates variability or a highly inverted spectrum, consistent with their findings.

0428+205: The optical host is a galaxy (19.3r magnitude at $z=0.219$) with emission extending from the center towards the SE and then NE, with an envelope of a rather triangular shape. Within a 10 arcsecond distance there are a few fainter objects. Based on high-frequency radio images or considering only the brightest components at lower frequency, this object would resemble the previous one, 0316+162, with two sides showing very different flux densities. Indeed, our reprocessed archive image at 1.2 GHz reveals an arc of faint emission extending to the east from the northern hot-spot/lobe and an emission extending west from the southern hot-spot, following an arc and then leading to East. This is corroborated by the 332 MHz image where

¹ ned.ipac.caltech.edu

Table 2. additional VLBA archive projects. Columns are: source name, observing frequency, project name, epoch of observation.

Source	ν_{GHz}	project	date
0108+388	15.36	BT030	03 Feb 1997
0316+162	0.609	BV014	23 Oct 1995
	2.29	UF001	12 Aug 2017
	4.98	BG239	14 Feb 2016
0428+205	0.332	BW067	02 Aug 2003
	2.29	BG219	23 Jan 2015
0941-080	1.41	BM185	26 Apr 2003
	2.29	UG002	08 Apr 2018
	8.30	BM185	26 Apr 2003
1031+567	1.41	BM185	26 Apr 2003
	4.95	BM185	26 Apr 2003
	"	BB131	16 Dec 2000
	8.30	BM185	26 Apr 2003
1117+146	2.27	BK095	10 Sep 2002
1323+321	1.67	BM125	08 Jul 2000
	8.30	BM125	08 Jul 2000
	4.54	BM125	08 Jul 2000
	15.36	BK068	04 Mar 2001
1358+624	0.611	BM102	27 Jun 1998
	1.41	BM102	27 Jun 1998
	4.98	UZ001	14 May 2017
	22.22	UZ001	14 May 2017
1404+286	1.460	BH104	09 Jan 2003
1607+268	1.63	BW138	22 Jan 2022
	2.30	BN025	25 Oct 2003
	4.99	BN025	25 Oct 2003
	8.42	BN025	25 Oct 2003
2128+048	2.30	BF071	31 Jan 2002
2342+821	1.29	GP021	23 Feb 1999
	2.28	BP222	01 Sep 2018
2352+495	1.41	BM185	26 Apr 2003
	2.28	BA064	17 Jan 2003

the lateral emission is much brighter. The 1.7 GHz image presented by Dallacasa et al. (1995) already shows some hints of the faint lateral emission. The high frequency images show the southern side in detail with a jet-like morphology terminating in a hot spot. Dallacasa et al. (2013) proposed component Ce1 as the source core based on the flat spectral index found between their 1.7 and 5 GHz VLBI data.

0500+019: The optical host is a slightly elongated object (21.0i magnitude at redshift 0.5845) surrounded by many other objects within a distance of 20 arcseconds. Our VLBA image at 8.42 GHz clearly shows an S-shaped emission, confirming the morphology presented by Stanghellini et al. (1997, 2001). At higher frequencies, the faint southern part is gradually resolved out. Pushkarev & Kovalev (2012) present an image at 2.3 GHz showing fainter emission extending west on the northern side, and extending east on the southern side.

0710+439: The optical host (20.4r magnitude at redshift 0.518) has an irregular, almost triangular shape, with a couple of compact components within the galactic envelope and several more objects within a distance of 20 arcseconds. The radio morphology consists of two hot spots and a central jet. Taylor et al. (1996) propose the southern tip of the central jet-like feature as the core. The images at low frequency show faint extended emission following an arc towards the west from the northern hot spot

and towards the east from the southern hot spot. A hint of this lateral emission is already seen in an image presented by Fey et al. (1996). An expansion speed of the hot-spots of 0.43c is detected by Polatidis & Conway (2003).

0941-080: The optical host is a galaxy (17.9r magnitude at redshift 0.228) with a double nucleus, with the AGN being associated with the northern one. The radio morphology consists of two main components with an arc shape. The emission extending from the southern component towards the center of activity can be separated in an additional compact component in the 8.3 GHz image.

1031+567: The optical host is a faint, slightly resolved object (20.2r magnitude at redshift 0.459) with a couple of other objects at a distance of 15 arcseconds. The closest unresolved bright object is likely a foreground star. The radio morphology consists of two bright hot-spots, a central compact component, and significantly extended emission elongating laterally and in opposite directions with respect to the two hot spots. The size of the lateral emission is comparable to the distance between the hot spots. A hint of this emission was already observed in an image at 2.3 GHz presented by Sokolovsky et al. (2011). Taylor et al. (1996) identify component C as the possible core, although doubts arise from its steep spectral index, which is also confirmed by our images. Polatidis & Conway (2003) report a relative proper motions of the two hot spots of 0.27c. This is a striking example of aligned morphology at high frequency, where only the brightest and recently active regions are visible but which shows much more complexity when sensitive observations at low frequency allow the detection of fainter emission.

1117+146: The optical host is a galaxy (20.1R magnitude at redshift 0.3632) with a couple of fainter objects within 10 arcseconds. The radio morphology shows a double structure with two bright hot spots at the outer edges and jet/lobes extending towards the center of activity. Sanghera et al. (1995) presented a global VLBI image at 1.6 GHz fully consistent with our images. Bondi et al. (1998) presented a MERLIN image at 23 GHz, showing a central component that is not seen at lower frequencies, which they identify as the core. Despite the high sensitivity of our 5 GHz image, we do not detect that compact component, implying that it is heavily self-absorbed and/or significantly variable in flux density, confirming its identification with the radio core. This radio source is the only one of our sample showing a clear scaled down FR II morphology.

1245-197: Despite the identification of the optical host with a quasar of 20.5V magnitude at redshift 1.275, the PanSTARRS image shows a faint object with a rather triangular shape. Other weakly resolved sources, probably galaxies, are present within a distance of 15 arcseconds. Sokolovsky et al. (2011) presented images at 2.3 and 8.4 GHz of this radio source resembling a double/triple radio source. Our high-sensitivity images reveal a different morphology. The main structure is seen in our 1.7 GHz image and consists of two regions of emission placed in the EW direction, 150 mas apart, with the eastern one being six times brighter. At higher frequencies, the western side is partially resolved out, whereas the eastern part shows an arc-like substructure, with a brighter component at one end and a trail of emission extending north and then bending east.

1323+321: The optical host is a galaxy (19.2r magnitude at redshift 0.369) surrounded by small objects within a distance of ~ 10 arcseconds, with a diffuse trail extending from south to east and then to north. The radio morphology consists of two hot spots prominent in the highest frequency images, with jet-like structures extending back towards the center of activity. At lower frequencies, we observe extended emission broaden-

Table 3. Flux density of components at different bands. The exact frequency is indicated for each data set as this may differ, within the same band, for different projects. Flux densities were calculated using the IMSTAT task in AIPS, except for some compact components, for which flux densities were derived with MODELFIT task in DIFMAP to better isolate their contribution from the surrounding diffuse emission. The spectral index was calculated between the two highest listed frequencies. The ratio between VLBA and VLA flux densities was determined at the lower listed frequency, interpolating the VLA flux density from Stanghellini et al. (1998) to match the exact VLBA frequency. An (x) indicates the component is not detected at that frequency, while the symbol (") indicates the flux density of that component is included in the component listed above.

Source	Comp	S_P	S_L	S_S	S_C	S_X	S_U	S_K	α_{thin}	S_{VLBA}/S_{VLA}
0019-000	ν_{GHz}		1.67		4.99	8.42				
	N		1677		634	367			1.04	
	S		715		231	122			1.22	
	tot		2392		865	485			1.11	0.93
0108+388	ν_{GHz}				4.89	8.30	15.36			
	E				766	586	271		1.25	
	Ce				x	x	15.1			
	W				496	326	85.3		2.18	
	tot				1260	912	371		1.46	0.98
0316+162	ν_{GHz}	0.609		2.29	4.98					
	N	7934		4232	1995				0.97	
	Ce1	x		x	36.3					
	Ce2	x		x	6.8					
	Ce3	130		33.9	9.6				1.62	
	tot	9539		4266	2072				0.93	1
0428+205	ν_{GHz}	0.332	1.16	2.29	4.99	8.42				
	N	1105	327	118	46.1	x				
	Ce1	x	x	40.4	26.5	16.9			0.92	
	Ce2	x	x	119	99.4	61.1			1.16	
	S	1365	2184	2909	1574	907			1.07	
	tot	2470	2511	3186	1746	985			1.10	0.93
0500+019	ν_{GHz}					8.42	15.36	22.23		
	N					452	244	192	0.65	
	Ce1					679	517	565	-0.24	
	Ce2					234	179	184	-0.07	
	S					140	50.9	31.5	1.3	
	tot					1505	991	972	0.05	1
0710+439	ν_{GHz}		1.64		4.89	8.30				
	N		1280		770	436			1.08	
	Ce		434		579	389			0.75	
	S		225		177	82.5			1.44	
	tot		1939		1526	908			0.98	0.99
0941-080	ν_{GHz}		1.41	2.29		8.30				
	NW		1269	792		156			1.26	
	SE		1149	744		165			1.17	
	tot		2418	1536		321			1.22	0.92
1031+567	ν_{GHz}		1.41	4.95	8.30					
	NE		1072	472	323				0.73	
	C		x	4.6	2.93				0.87	
	SW		772	607	401				0.80	
	tot		1844	1084	727				0.77	1
1117+146	ν_{GHz}			2.27	4.99					
	NW			653	355				0.77	
	SE			845	450				0.80	
	tot			1498	805				0.79	0.89
1245-197	ν_{GHz}		1.67		4.99	8.42				
	W		578		84.2	40.7			1.39	
	E		3284		1521	821			1.18	
	tot		3862		1605	862			1.19	0.83

Table 4. Flux density of components (continue)

Source	Comp	S_P	S_L	S_S	S_C	S_X	S_U	S_K	α_{high}	S_{VLBA}/S_{VLA}
1323+321	ν_{GHz}		1.67		4.54	8.30	15.36			
	NW		2152		1310	601	435		0.53	
	C		x		16.7	7.3	9.7		-0.46	
	SE		1625		844	310	191		0.79	
	tot		3777		2171	918	634		0.6	0.86
1345+125	ν_{GHz}		1.67			8.42	15.36			
	N		95.2			36.7	24.8		0.65	
	C		213			292	220		0.47	
	S		4264			734	360		1.19	
	tot		4572			1063	603		0.94	0.94
1358+624	ν_{GHz}	0.611	1.41		4.98			22.22		
	E	3597	2813		983			142	1.27	
	C	x	x		20.1			32.9	-0.33	
	W	2290	1560		346			43.8	1.38	
	tot	5816	4373		1349			219	1.22	0.99
1404+286	ν_{GHz}		1.46			8.42	15.36			
	E		829			1815	1005		0.98	
	W		"			146	57.6		1.55	
	Ce		x			x	3.7			
	D		29.0			x	x			
tot		855			1961	1067		1.01	0.99	
1518+047	ν_{GHz}		1.67		4.99	8.42				
	N		1969		392	138			2.0	
	S		1335		479	192			1.75	
	tot		3304		871	330			1.86	0.95
1607+268	ν_{GHz}		1.63	2.30	4.99	8.42				
	N		2401	1846	879	478			1.16	
	S		1841	1524	682	327			1.41	
	tot		4254	3370	1558	804			1.26	0.96
2008-068	ν_{GHz}				4.99	8.42	15.36			
	N				1089	687	366		1.05	
	Ce				12.4	9.9	6.7		0.65	
	S				132	68.3	26.9		1.55	
tot				1233	765	405		1.06	0.94	
2128+048	ν_{GHz}			2.30		8.42	15.36			
	N			2272		1034	431		1.46	
	Ce			15		16	7		1.38	
	S			319		67	16		2.38	
tot			2606		1117	447		1.52	0.83	
2210+016	ν_{GHz}		1.67		4.99	8.42				
	W		731		222	114			1.27	
	E		1268		540	251			1.46	
tot		1988		762	365			1.41	0.81	
2342+821	ν_{GHz}		1.29	2.28						
	W		3193	1944					0.87	
	Ce		182	117					0.78	
	E		95	53					1.02	
tot		3478	2110					0.88	0.87	
2352+495	ν_{GHz}		1.41	2.29	4.89	8.30				
	N		600	397	188	115			0.93	
	S		667	451	206	113			1.14	
	Ce		1172	998	874	702			0.41	
	C		"	20	30	32			-0.12	
tot		2452	1871	1297	966			0.56	0.95	

ing transversely to the hot spot positions, reaching a size almost comparable to the distance between the two hot spots. This lateral extended emission is already visible in an image at 2.3 GHz presented by Fey et al. (1996). Tremblay et al. (2016) identify a flat spectrum core coincident with component C in our images. The spectral index of the core calculated from our images is not reliable due to its faintness. Kellermann et al. (2004) find no evidence of relative proper motion of the two hot spots.

1345+125: The optical host is an ultraluminous infrared galaxy (ULIRG) of 15.5r magnitude at a redshift of 0.122. It presents a double nucleus, irregular shape, trails, and tails, which are clear signatures of an ongoing merger. Stanghellini et al. (1993) associate the radio source with the western nucleus, a conclusion confirmed by Axon et al. (2000) using HST observations. Scoville et al. (2000) discuss infrared NICMOS observations, and find the western nucleus unresolved and much redder than the eastern one, which is also extended. Emons et al. (2016) present detailed optical images and conclude that a major, possibly multiple merger event is currently ongoing.

The radio morphology consists of a bright and heavily bent southern jet terminating in a hot spot and surrounded by a lobe, and a much fainter northern lobe. The radio core is associated with component C (Stanghellini et al. 2001; Xiang et al. 2002; Lister et al. 2003). Lister et al. (2003) estimate a jet speed close to the core of $0.84c$ and a viewing angle of 64° . Morganti et al. (2013) find a fast outflow of cold gas (HI) associated with the southern hot spot. Stanghellini et al. (2005) report the detection of faint emission at the arcsecond scale, considered as a relic of the past radio activity of the AGN.

1358+624: The host galaxy (19.8r magnitude at redshift 0.4291) has a boxy morphology with a hint of a transverse band of optical absorption. Another object with a slightly elongated morphology is located 5 arcseconds to the north. The radio morphology consists of a knotty and bright jet on the SE side, terminating in a hot spot, with fainter extended emission further along the jet direction and south of the hot spot. The NW side has a hot spot with additional emission that extends north, broadens, and bends to the east. The compact component C has an inverted spectrum and is identified as the core, which confirms earlier works by Taylor et al. (1996) and Dallacasa et al. (2013).

1404+286: The optical host is a broad-line radio galaxy (BLRG) of 14.6r magnitude at redshift 0.077. It has a disk morphology with multiple compact components within the common envelope and a trail of emission bending from north to east. The radio morphology consists of a brighter eastern component and a much fainter western component. The eastern component exhibits substructure with transverse emission relative to the radio source axis and additional emission extending towards the center. The western side comprises two similar components. We identify the brightest eastern and western components as the two hot spots of a double source. Very faint emission is detected 30 mas west of the main structure at 1.7 GHz, and there is a hint of emission between the two hot spots. Wu et al. (2013) also report faint components between the hot spots, not always visible at different epochs, and a separation speed of $0.134c$ for the two hot spots, with evidence of sideways motions.

1518+047: The optical host is a faint galaxy (22.6r magnitude at redshift 1.296) surrounded by objects with similar magnitude within 10 arcseconds. The radio morphology consists of two bright hot spots with additional emission extending outwards from the northern hot spot and towards the center from the southern hot spot. Orienti et al. (2010b) report no evidence of injection of new electron injection in the hot spots, suggesting that this object is a dying radio source.

1607+268: The optical host is a faint and roughly triangular object (20.4r magnitude at redshift 0.473) with a couple of objects within 10 arcseconds. The radio morphology consists of a double structure, with diffuse emission extending south from the northern hot spot, then bending to the west. The southern side shows a jet terminating in a hot spot with additional emission elongating laterally toward the east.

2008-068: The optical host is a faint object (20.9i magnitude at redshift 0.547) with an irregular double structure. The radio morphology consists of a brighter northern hot spot and a fainter southern one. Additional radio emission extends from the two hot spots at an angle of $\sim 45^\circ$ with respect to the radio source axis. A compact component is present at the center of the structure, with a flatter spectral index compared to the other components, but it is still too steep to confidently identify it as the core.

2128+048: The optical host (23.3r magnitude at redshift 0.99) has a double morphology with two weak components at a distance of 5 arcseconds, with the radio source coincident with the peak of the northern optical emission. The radio morphology consists, similar to the previous object, of a brighter northern hot spot and fainter southern one. Again, emission extends from the hot-spots at an angle of $\sim 45^\circ$ with respect to the radio source axis, then bends towards the center of the radio source. There are also a couple of compact components between the two hot spots, none of which have a flat spectrum, and a bent jet connecting the northern compact component to the northern hot spot. The southern hot spot is surrounded by emission bending towards the west. The radio morphology of this source was investigated by Stanghellini et al. (1997) at 5 GHz, showing a structure similar to our images, and by Dallacasa et al. (1998), where the strongest components are visible at a lower angular resolution.

2210+016: The optical host is a faint object of 21.7r magnitude at redshift 1.126. The radio morphology is quite complex. A compact but resolved component, probably a hot spot, is located at the western edge of the radio source. A jet extends eastwards from the center of the radio source, then broadens towards south-east.

2342+821: The optical host is identified as a quasar with a magnitude of 20.1r at a redshift of 0.735. A few faint objects are present within 10 arcseconds. The radio structure consists of three main components. The component at the western edge features a bright hot spot surrounded by lobe emission. The other two fainter components, located at the center and the eastern edge, each exhibits a double substructure. The image at 327 MHz presented by Dallacasa et al. (2021) shows additional extended emission between components E and Ce.

2352+495: The optical host is a galaxy with a magnitude of 18.4R at a redshift of 0.2379. It has an irregular, somewhat triangular shape with hints of diffuse emission around the main structure and several objects within 10 arcseconds. The radio morphology consists of two bright hot spots. The extended emission laterally elongates from the southern hot spot, while it follows an arc from the northern hot spot. From the bright central component, there is emission extending northward and a long curved jet connecting the center to the southern hot spot. Taylor et al. (1996) identify component C in our images as the core, and we also confirm this identification given its compactness and flat spectral index. Polatidis & Conway (2003) estimate a separation speed of $0.17c$ for the two hot spots. The central region observed by Taylor et al. (2000) shows a complex structure in which five components have velocities ranging from 0.27 to $0.76c$.

5. Discussion

5.1. Radio and optical Morphology

Seventeen of the 21 objects in our sample show indication compatible with jet precession or relative motion between the AGN and the ISM. Four objects lack such evidence. Therefore, less than 20% exhibit an aligned morphology. This fraction might be even lower, as these objects could be reclassified if additional extended emission is detected at lower frequencies or with more sensitive observations, as was the case for 0428+205 and 0710+439.

The presence of an S-shaped morphology in CSOs has been previously noted by Taylor et al. (1996) as indicative of ongoing jet precession. This phenomenon was studied in more detail by Readhead et al. (1996b) in the case of 2352+495, who, however, favored a young age for this radio source.

In our sample, only about half a dozen objects show a core or a candidate core, confirming that flat-spectrum cores are mostly undetected in JSS radio sources at the frequencies and sensitivities of the currently available observations.

Despite the limited statistics, we observe a clear difference in the (projected) linear size between sources with and without indication of jet redirection. The former are more compact, usually < 1 kpc (Fig. 1), with no evident difference in the luminosity distribution (Fig. 2).

Among the 17 objects exhibiting jet precession signatures, we have 10 cases where the host galaxy is observed with a $S/N > 50$, enabling the detailed observation of several features. None of these 10 galaxies is a typical elliptical galaxy. All of them exhibit disturbed optical morphologies and have nearby fainter objects within a few arcseconds. Five of these galaxies show double nuclei or multiple compact components within the same optical envelope. Others show varying degrees of morphological disturbances (tails, arms, boxy/triangular shapes), indicative of current or recent mergers (e.g. Pawlik et al. 2016).

It is well established that GPS radio galaxies reside in optically disturbed or merging systems (O’Dea & Saikia 2021, and references therein), but it was not previously demonstrated that they differ significantly from the hosts of their larger counterparts. In a recent study, Meusinger & Mhaskey (2024) found a significantly higher fraction of mergers in their sample of PSS-CSO ($\sim 60\%$) compared to their control sample of large radio galaxies ($\sim 15\%$). Our results are fully consistent with their findings. Based on the merger fractions in their samples, they also concluded that only half of peaked sources are expected to evolve into large radio galaxies.

5.2. A novel interpretation

The morphology observed in most JSS radio sources is naturally explained by a jet precessing rapidly at large angle (i.e., $> 10^\circ$), with a fainter emission trail transverse to the hot spot indicating the past position of the hot spot. The presence of arc segments, clearly visible in some objects (i.e. 0941-080, 1245-197), further supports the hypothesis of a precessing jet. In the case of radio sources with transverse lobes that extend on the same side (T_S marker), the dominant effect might be the motion of the black hole through the ISM.

Based on the radio and optical morphologies described above, we propose a scenario in which radio sources originating in galaxies undergoing a merging phase might be confined (frustrated) within the galaxy core by jet redirection resulting from a combination of jet precession and the orbital motion of

the AGN producing the jet. Our scenario is illustrated in Fig. 3, in the idealized case of precession-driven morphology only (Fig. 3a, 3b, 3c, and 3d or orbital-driven morphology only (Fig. 3e).

In a merging system, large regions of gas might be in relative motion with respect to the general gravitational potential well, contributing to the relative motion between the hot spots and the environment. The dynamically active gas and its inhomogeneous distribution in a merging system can lead to complex radio morphologies, characterized by significant differences in size, shape, and brightness between the two opposite sides of the radio source relative to their central origin.

The morphology seen in our images suggests that the hot spot, in its lateral motion, traverses a path comparable to the size of the radio source. Consequently, a jet that continuously changes the direction and location of its terminal shock does not have time to push the gas forward and expand rapidly outward.

In the following, we will critically discuss our scenario based on observational evidence.

5.3. Proper and transverse motions

Several objects have measured proper motions of the hot spots expanding outwards (Polatidis & Conway 2003; Gugliucci et al. 2005; An & Baan 2012), suggesting, contrary to our hypothesis, that at least for those sources, the youth scenario is the most likely explanation. O’Dea & Saikia (2021) list 42 objects with measured proper motions, including 9 with only an upper limit (excluding proper motions of inner knots). Six of these objects are part of our sample: 0108+388, 0710+439, 1031+567, 1404+286, 1607+268, and 2352+495. Regarding 1404+286, Wu et al. (2013) report a complex relative motion of the hot spots with a transverse component. Polatidis & Conway (2003) also report an unusual side motion for 0108+388 and 1031+567, which they attribute to the *dentist’s drill effect* (Scheuer 1982). Cassaro (2020) tentatively finds oscillation on the distance of the two hot-spots over time for 1031+567. Additionally, a revision of the proper motion of 2352+495 indicates a transverse relative displacement of the hot spots (Stanghellini et al. in prep.). It appears that most objects with detected proper motions may need a revision, focusing on a more precise determination of the lateral displacements of the jet terminations.

Transverse motions, or more precisely, transverse displacements of the termination of the jet (in our precessing scenario, the hot spot does not actually have dynamic motion), have also been detected in some JSS radio sources not included in our sample. Stanghellini et al. (2009b) report transverse displacement for three JSS radio sources and suggest jet precession as the cause. An et al. (2012) confirm the transverse displacement in one of the objects mentioned above and find more evidence in two additional cases.

In our scenario, when jet precession is the dominant cause of the changing direction of the jet, we may expect displacement vector components both transverse to and along the jet axis due to projection effects (Fig. 3a,b,c). Therefore, the proper motions reported in literature, even when confirmed, are not inconsistent with our scenario (Fig. 3b). Indeed, we should expect some sources to appear to be shrinking (Fig. 3c), and some examples have been reported. An et al. (2012) find a decreasing distance with time in one object they observed (J0017+5312), although the classification of this object as a JSS radio source is uncertain. Another intriguing example of a shrinking radio source is PKS 1155+251 (Tremblay et al. 2008; Yang et al. 2017), but in this case, the contraction cannot be explained simply by precession and likely requires, within our scenario, a combination of

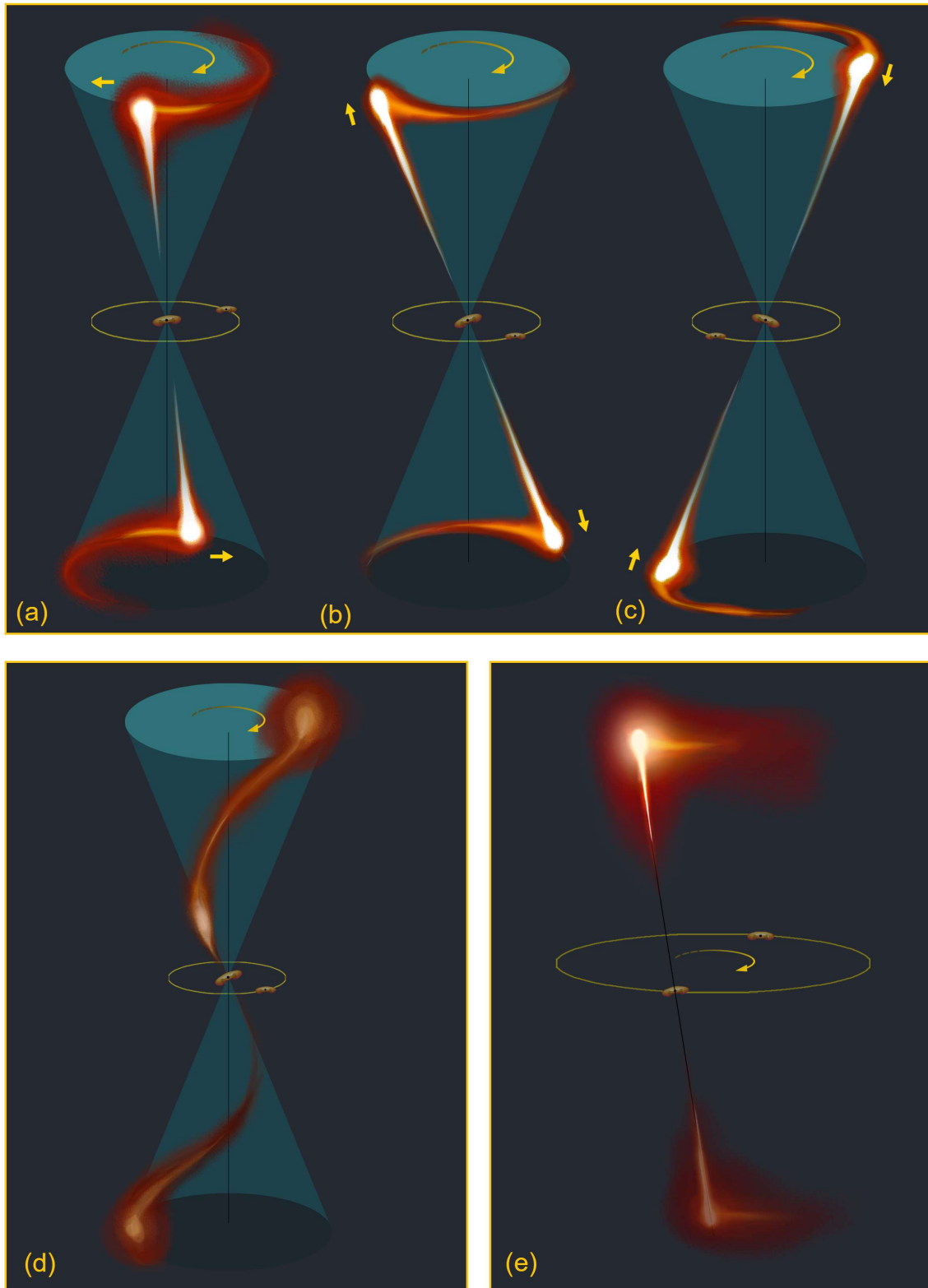


Fig. 3. Jet redirection scenario. The proposed scenario (Sect. 5.2) is simplified here. *Top row:* Panels a, b, and c represent cases where jet precession solely causes the observed morphology, with transverse (a), expansion (b), or contraction (c) motions on the plane of the sky being effects of geometry and projection. *Bottom row:* Panel (d) represents the case of a precessing jet with a period shorter than (or comparable to) the travel time of the jet from the core to the hot spot, resulting in an S-shaped morphology. Panel (e) illustrates a scenario where the orbital motion of the radio-loud AGN, with a random inclination of the jet axis relative to the orbital plane, is solely responsible for the observed morphology. Actual cases may involve a combination of these two phenomena, jet-driven morphology and orbital-driven morphology, with one predominating over the other. Distance, size, and shape of the SMBHs are not to scale and are for illustrative purposes only [Illustration by Luca Jerrert Rossi].

precession and orbital motion of the AGN in a dual black hole system.

A larger number of JSS radio sources with measured proper motions/displacements are needed to conduct a statistically robust study and place solid constraints on our hypothesis.

5.4. Jet precession at different scales

Lobe asymmetries, trails in different directions, curved jets, S-shaped jets are often seen in large radio galaxies, with the most likely explanation being a precessing jet. Krause et al. (2019) found strong evidence for jet precession in three-quarters of their studied sample of FR II radio galaxies. Therefore, the presence of a precessing jet alone is not sufficient to keep the radio source small.

Precessing jets in *large* radio galaxies have recently been modeled by Nolting et al. (2023), who found that different precession parameters significantly change the size of a radio galaxy at a given time. In particular, jets precessing at a large angle can significantly slow down the overall growth of the radio source. Thus, the precession angle is an important parameter in determining the growth and expansion of the radio source, with precession at large angles keeping the radio source more compact.

The precession period may be even more important in influencing the size of the radio source. 3D hydrodynamical simulations by Horton et al. (2020) show that a shorter precession period causes the radio source to grow at a slower rate. The arc features and lobe extensions seen in the simulated images (Fig. 2 of Horton et al. 2020) are similar to the arc features and transverse lobes observed in our images.

Krause et al. (2019) estimate that the jet precession period in their sample of 3CR radio galaxies is between $10^6 - 10^7$ yr.

The best case of measured transverse motion in JSS is J1335+5844, detected by Stanghellini et al. (2009b) and confirmed by An et al. (2012). The transverse displacement estimated using the values in Table 1 of An et al. (2012) corresponds to a projected angular velocity for the jet axis of $4.2(\pm 1.2)$ arcminutes per year ($0.016/2$ mas/yr for the hot spot displacement), resulting in a period of $\lesssim 2 \times 10^3$ yr, assuming a cone of 45° for the precession. Similar precessing periods may be estimated with less accuracy for the other few objects showing transverse motions, e.g. J0706+4647 and J1823+7938 in Stanghellini et al. (2009b).

With the caveat of high uncertainty and low statistics, it seems that the precession period of the jet axis in a JSS radio source is 10^{2-3} shorter than in FR II radio sources.

Is this short period possible? Krause et al. (2019) discussed the possible causes of precession. Geodetic precession predicts a much longer precession than is consistent with our scenario. Geodetic precession would require an unrealistic distance between the black holes to allow for a 10^4 year period, as it would place the binary SMBH in the gravitational-wave regime, leading to fast coalescence. On the other hand, precession induced by an irregular or warped accretion disk would last for only one period and quickly disappear. Lobanov & Roland (2005) predict a precession period of a few 10^3 years in the case of 3C345, with the precession caused by the orbital motion of the secondary on the accretion disk of the active black hole. Therefore, there is at least one physical mechanism capable of explaining the precession period we see in JSS radio sources. However, determining the actual cause of the jet precession is beyond the scope of this paper.

In our scenario, radio sources may be kept compact when the precession angle is large and the precession period is short.

The comparison of the time necessary for the relativistic plasma to reach the hot spot from the core with the precession period determines the observed morphology: if the former is much smaller than the latter, we get straight jets; otherwise, they will appear S-shaped (Krause et al. 2019).

5.5. Binary supermassive black holes and their orbital motion

As an intermediate phase of the merging process, we expect pairs of SMBHs. Following the nomenclature of De Rosa et al. (2019) we refer to *dual* AGN if the two active SMBHs are separated by more than 1 pc, while the pairs at separations < 1 pc are *binary* AGN systems.

After a galaxy merger, the orbital periods of surviving binary black holes are in the range $10-10^5$ yr (Yu 2002). Interestingly, this range is consistent with the estimated radiative ages for electrons in the lobes of JSS radio sources, which is the age of the oldest detectable radio emission, while the radio source itself may be older.

Chen et al. (2020) find that the coalescence timescales of binary black holes are in a range 10^8-10^{12} yr. This means that, if a radio source cannot expand due to the presence of a dual/binary black hole, it may stay compact for a timescale comparable to the life time of a large extragalactic radio source, or even indefinitely, potentially explaining the relative significant number of JSS radio sources.

The orbital motion of a dual or binary black hole may be another factor contributing to the small size of the radio source, as the relative motion of the black hole and the ISM may cause the terminal shock of the jet to continuously shift the impact direction. Morphologies showing transverse lobes or trails on the same side of the radio source axis may be the cases where this phenomenon dominates (Fig. 3e). This phenomenon, observed on a smaller scale, is similar to the narrow-angle tail (NAT) radio galaxies seen in galaxy clusters. The long tails characteristic of NATs are absent in these cases due to the shorter path length and a much shorter radiative age caused by the stronger magnetic fields in the inner galaxy (see also Sect. 5.6).

Bansal et al. (2017) calculated the orbital period of the dual black hole system in the CSO 0402+379 to be 3×10^4 years. Remarkably, this orbital motion period is of same order, or within an order of magnitude, as the precession periods in JSS radio sources discussed above. Therefore, it is not surprising that they may produce similar effects on the morphology.

Deane et al. (2014) confirmed that J1502+1115 is a triple supermassive black hole system with a distance of 140 pc for the closest pair, which is 20 times the separation of the black holes in the system studied by Bansal et al. (2017). They also revealed an S-shaped radio emission centered on that pair, attributed to jet precession, extending for ~ 10 kpc. This is a larger size compared to the objects in our sample, but still within the host galaxy. This latter case supports the connection between dual black holes and radio compactness, making it important to extend our study to larger JSS radio sources.

5.6. Radiative ages and old radio emission

In the radio source 1323+321 from our sample, Murgia (2003) calculates the radiative age from the fit along the lobes. While the purpose of that paper is to compare radiative ages with dynamical ages, assuming the radio source expands along the jet axes, it is noteworthy that the figures and plots (Fig. 4) show the radiative age also increasing along the transverse trail of the

southern hot spot. This could be due to aging of the backflow from the hot spot, as seen in many extended radio galaxies, but it could also indicate that the hot spot was previously located there. Considering a displacement of the hot spot of 10 mas in 2000 years, the jet would be precessing with a projected angular velocity of 0.3 arcminute/yr, consistent with the few estimated angular velocities (Sect. 5.4).

For the other objects in our sample, we lack sufficient and/or reliable multifrequency data with matched UV coverage. This matched UV coverage is necessary to achieve comparable angular resolution and sensitivity to extended emission, which would allow us to estimate the radiative age along the trails/lobes.

If the radio source spends a long time in the central part of the host galaxy with its precessing jet, there should be residual emission forming a halo or cocoon around the active regions. With magnetic fields of a few to several tens of mGauss (Oriente 2016), the break frequency would shift below 100 MHz in a few thousands years, making it generally undetectable in much older radio sources at typical observing frequencies. Occasionally, this diffuse emission can be observed, as in the case of the lowest redshift object in our sample, 1404+286, where faint emission at mas scale beyond the double structure has been reported and confirmed (Wu et al. 2013). Recent EVN+eMERLIN observations have detected even more diffuse emission around the double structure, consistent with our scenario (Stanghellini et al. in prep.).

6. Conclusions

We performed a radio and morphological study of a sample of JSS radio sources, finding that the radio structure often show signatures of precessing jets at large angles or in motion with respect to the ISM, and the optical hosts often appear as merging systems. We suggest that JSS radio galaxies consist of a mixed class of objects, with a minority of aligned sources, which will likely expand to become FRI/II radio galaxies. The majority of the radio sources, showing complex morphologies, may contain a rapidly precessing jet and/or an AGN moving respect the ISM (orbital motion of the AGN or dynamical motion of the gas during the merger), keeping them confined into the inner region of the host galaxy, and making them "frustrated" objects.

We propose a scenario where these JSS radio sources are in merging systems, possessing dual or binary black hole systems, and remain at parsec scale for a prolonged time due to the continuous redirection of the jet. Asymmetries in size and flux densities may result from a combination of factors: moderate relativistic beaming, inhomogeneous ISM distribution, orbital motion of the active SMBH, and relative motion of the hot spots with respect to the ISM.

The possibility that a fraction of JSS radio sources are short-lived objects is not inconsistent with our scenario. In a galaxy merger, the environment surrounding the SMBH may be dynamically heavily disturbed, and the reservoir of accreting material (gas or stars) may vary greatly over time, with short episodes of activity, and the radio source possibly switching on and off.

Refined analysis and, especially, specific modeling and numerical simulations are needed to confirm that our scenario is physically consistent. If our scenario is correct, we expect to find more examples of transverse motions and more evidence of old emissions tracing the path of the precessing jet. JSS radio sources may be the objects to preferentially look for in the hunt for binary black holes.

Acknowledgements. We thank Luca Jerrert Rossi (jerrert@gmail.com) for creating the drawing used in this paper. CO and SB acknowledge support from

the Natural Sciences and Engineering Research Council (NSERC) of Canada. CS acknowledges financial support from the Italian National Institute for Astrophysics (INAF, FO: 1.05.12.04.04). MPT acknowledges financial support from the Severo Ochoa grant CEX2021-001131-S and from the National grant PID2020-117404GB-C21, funded by MCIU/AEI/10.13039/501100011033. The National Radio Astronomy Observatory is a facility of the National Science Foundation operated under cooperative agreement by Associated Universities, Inc. This research has made use of the NASA/IPAC Extragalactic Database, which is funded by the National Aeronautics and Space Administration and operated by the California Institute of Technology. Based on observations made with the Nordic Optical Telescope, owned in collaboration by the University of Turku and Aarhus University, and operated jointly by Aarhus University, the University of Turku and the University of Oslo, representing Denmark, Finland and Norway, the University of Iceland and Stockholm University at the Observatorio del Roque de los Muchachos, La Palma, Spain, of the Instituto de Astrofísica de Canarias. The Pan-STARRS1 Surveys (PS1) and the PS1 public science archive have been made possible through contributions by the Institute for Astronomy, the University of Hawaii, the Pan-STARRS Project Office, the Max-Planck Society and its participating institutes, the Max Planck Institute for Astronomy, Heidelberg and the Max Planck Institute for Extraterrestrial Physics, Garching, The Johns Hopkins University, Durham University, the University of Edinburgh, the Queen's University Belfast, the Harvard-Smithsonian Center for Astrophysics, the Las Cumbres Observatory Global Telescope Network Incorporated, the National Central University of Taiwan, the Space Telescope Science Institute, the National Aeronautics and Space Administration under Grant No. NNX08AR22G issued through the Planetary Science Division of the NASA Science Mission Directorate, the National Science Foundation Grant No. AST-1238877, the University of Maryland, Eotvos Lorand University (ELTE), the Los Alamos National Laboratory, and the Gordon and Betty Moore Foundation. Funding for the Sloan Digital Sky Survey V has been provided by the Alfred P. Sloan Foundation, the Heising-Simons Foundation, the National Science Foundation, and the Participating Institutions. SDSS acknowledges support and resources from the Center for High-Performance Computing at the University of Utah. SDSS telescopes are located at Apache Point Observatory, funded by the Astrophysical Research Consortium and operated by New Mexico State University, and at Las Campanas Observatory, operated by the Carnegie Institution for Science. The SDSS web site is www.sdss.org. SDSS is managed by the Astrophysical Research Consortium for the Participating Institutions of the SDSS Collaboration, including Caltech, The Carnegie Institution for Science, Chilean National Time Allocation Committee (CNTAC) ratified researchers, The Flatiron Institute, the Gotham Participation Group, Harvard University, Heidelberg University, The Johns Hopkins University, L'Ecole polytechnique fédérale de Lausanne (EPFL), Leibniz-Institut fuer Astrophysik Potsdam (AIP), Max-Planck-Institut fuer Astronomie (MPIA Heidelberg), Max-Planck-Institut fuer Extraterrestrische Physik (MPE), Nanjing University, National Astronomical Observatories of China (NAOC), New Mexico State University, The Ohio State University, Pennsylvania State University, Smithsonian Astrophysical Observatory, Space Telescope Science Institute (STScI), the Stellar Astrophysics Participation Group, Universidad Nacional Autónoma de México, University of Arizona, University of Colorado Boulder, University of Illinois at Urbana-Champaign, University of Toronto, University of Utah, University of Virginia, Yale University, and Yunnan University.

References

- Abdurro'uf, Accetta, K., Aerts, C., et al. 2022, *ApJS*, 259, 35
 An, T. & Baan, W. A. 2012, *ApJ*, 760, 77
 An, T., Wu, F., Yang, J., et al. 2012, *ApJS*, 198, 5
 Axon, D. J., Capetti, A., Fanti, R., et al. 2000, *AJ*, 120, 2284
 Bansal, K., Taylor, G. B., Peck, A. B., Zavala, R. T., & Romani, R. W. 2017, *ApJ*, 843, 14
 Baum, S. A., O'Dea, C. P., Murphy, D. W., & de Bruyn, A. G. 1990, *A&A*, 232, 19
 Bicknell, G. V., Dopita, M. A., & O'Dea, C. P. O. 1997, *ApJ*, 485, 112
 Bondi, M., Garrett, M. A., & Gurvits, L. I. 1998, *MNRAS*, 297, 559
 Bronzini, E., Migliori, G., Vignali, C., et al. 2024, *arXiv e-prints*, [arXiv:2401.16479](https://arxiv.org/abs/2401.16479)
 Cassaro, P. 2020, in *Perseus in Sicily: From Black Hole to Cluster Outskirts*, ed. K. Asada, E. de Gouveia Dal Pino, M. Giroletti, H. Nagai, & R. Nemmen, Vol. 342, 237–238
 Chambers, K. C., Magnier, E. A., Metcalfe, N., et al. 2016, *arXiv e-prints*, [arXiv:1612.05560](https://arxiv.org/abs/1612.05560)
 Chen, Y., Yu, Q., & Lu, Y. 2020, *ApJ*, 897, 86
 Cotton, W. D., Dallacasa, D., Fanti, C., et al. 2003, *PASA*, 20, 12
 Czerny, B., Siemiginowska, A., Janiuk, A., Nikiel-Wroczyński, B., & Stawarz, L. 2009, *ApJ*, 698, 840
 Dallacasa, D., Bondi, M., Alef, W., & Mantovani, F. 1998, *A&AS*, 129, 219

- Dallacasa, D., Fanti, C., Fanti, R., Schilizzi, R. T., & Spencer, R. E. 1995, *A&A*, 295, 27
- Dallacasa, D., Orienti, M., Fanti, C., & Fanti, R. 2021, *MNRAS*, 504, 2312
- Dallacasa, D., Orienti, M., Fanti, C., Fanti, R., & Stanghellini, C. 2013, *MNRAS*, 433, 147
- Dallacasa, D., Stanghellini, C., Centonza, M., & Fanti, R. 2000, *A&A*, 363, 887
- De Rosa, A., Vignali, C., Bogdanović, T., et al. 2019, *New A Rev.*, 86, 101525
- Deane, R. P., Paragi, Z., Jarvis, M. J., et al. 2014, *Nature*, 511, 57
- Emonts, B. H. C., Morganti, R., Villar-Martín, M., et al. 2016, *A&A*, 596, A19
- Fanti, C., Branchesi, M., Cotton, W. D., et al. 2004, *A&A*, 427, 465
- Fanti, C., Fanti, R., Dallacasa, D., et al. 1995, *A&A*, 302, 317
- Fanti, C., Pozzi, F., Fanti, R., et al. 2000, *A&A*, 358, 499
- Fanti, R., Fanti, C., Schilizzi, R. T., et al. 1990, *A&A*, 231, 333
- Fey, A. L., Boboltz, D. A., Charlot, P., et al. 2002, in *American Astronomical Society Meeting Abstracts*, Vol. 201, American Astronomical Society Meeting Abstracts, 76.11
- Fey, A. L., Clegg, A. W., & Fomalont, E. B. 1996, *ApJS*, 105, 299
- Frey, S. & Titov, O. 2021, *Research Notes of the American Astronomical Society*, 5, 60
- Gopal-Krishna, Patnaik, A. R., & Steppe, H. 1983, *A&A*, 123, 107
- Greisen, E. W. 1990, in *Acquisition, Processing and Archiving of Astronomical Images*, 125–142
- Gugliucci, N. E., Taylor, G. B., Peck, A. B., & Giroletti, M. 2005, *ApJ*, 622, 136
- Horton, M. A., Krause, M. G. H., & Hardcastle, M. J. 2020, *MNRAS*, 499, 5765
- Kellermann, K. I., Lister, M. L., Homan, D. C., et al. 2004, *ApJ*, 609, 539
- Kiehlmann, S., Lister, M. L., Readhead, A. C. S., et al. 2024a, *ApJ*, 961, 240
- Kiehlmann, S., Readhead, A. C. S., O’Neill, S., et al. 2024b, *ApJ*, 961, 241
- Krause, M. G. H., Shabala, S. S., Hardcastle, M. J., et al. 2019, *MNRAS*, 482, 240
- Labiano, A., O’Dea, C. P., Gelderman, R., et al. 2005, *A&A*, 436, 493
- Labiano, A., Vermeulen, R. C., Barthel, P. D., et al. 2006, *A&A*, 447, 481
- Lister, M. L., Kellermann, K. I., Vermeulen, R. C., et al. 2003, *ApJ*, 584, 135
- Lobanov, A. P. & Roland, J. 2005, *A&A*, 431, 831
- Marecki, A., Barthel, P. D., Polatidis, A., & Owsianik, I. 2003, *PASA*, 20, 16
- Meusinger, H. & Mhaskey, M. 2024, *A&A*, 682, A18
- Morganti, R., Fogasy, J., Paragi, Z., Oosterloo, T., & Orienti, M. 2013, *Science*, 341, 1082
- Morganti, R. & Oosterloo, T. 2018, *A&A Rev.*, 26, 4
- Morganti, R., Oosterloo, T. A., Tadhunter, C. N., et al. 2004, *A&A*, 424, 119
- Murgia, M. 2003, *PASA*, 20, 19
- Nolting, C., Ball, J., & Nguyen, T. M. 2023, *ApJ*, 948, 25
- O’Dea, C. P. 1998, *PASP*, 110, 493
- O’Dea, C. P. & Baum, S. A. 1997, *AJ*, 113, 148
- O’Dea, C. P., Baum, S. A., & Stanghellini, C. 1991, *ApJ*, 380, 66
- O’Dea, C. P. & Saikia, D. J. 2021, *A&A Rev.*, 29, 3
- O’Dea, C. P., Worrall, D. M., Tremblay, G. R., et al. 2017, *ApJ*, 851, 87
- Orienti, M. 2016, *Astronomische Nachrichten*, 337, 9
- Orienti, M. & Dallacasa, D. 2008, *A&A*, 479, 409
- Orienti, M. & Dallacasa, D. 2020, *MNRAS*, 499, 1340
- Orienti, M., Dallacasa, D., & Stanghellini, C. 2007, *A&A*, 475, 813
- Orienti, M., Dallacasa, D., & Stanghellini, C. 2010a, *MNRAS*, 408, 1075
- Orienti, M., Murgia, M., & Dallacasa, D. 2010b, *MNRAS*, 402, 1892
- Ostorero, L., Moderski, R., Stawarz, L., et al. 2010, *ApJ*, 715, 1071
- Pawlik, M. M., Wild, V., Walcher, C. J., et al. 2016, *MNRAS*, 456, 3032
- Polatidis, A. G. & Conway, J. E. 2003, *PASA*, 20, 69
- Principe, G., Di Venere, L., Orienti, M., et al. 2021, *MNRAS*, 507, 4564
- Pushkarev, A. B. & Kovalev, Y. Y. 2012, *A&A*, 544, A34
- Readhead, A. C. S., Ravi, V., Blandford, R. D., et al. 2024, *ApJ*, 961, 242
- Readhead, A. C. S., Ravi, V., Blandford, R. D., et al. 2023, *arXiv e-prints*, arXiv:2303.11361
- Readhead, A. C. S., Taylor, G. B., Pearson, T. J., & Wilkinson, P. N. 1996a, *ApJ*, 460, 634
- Readhead, A. C. S., Taylor, G. B., Xu, W., et al. 1996b, *ApJ*, 460, 612
- Readhead, A. C. S., Xu, W., Pearson, T. J., Wilkinson, P. N., & Polatidis, A. G. 1994, in *Compact Extragalactic Radio Sources*, ed. J. A. Zensus & K. I. Kellermann, 17
- Reynolds, C. S. & Begelman, M. C. 1997, *ApJ*, 487, L135
- Rossetti, A., Dallacasa, D., Fanti, C., Fanti, R., & Mack, K. H. 2008, *A&A*, 487, 865
- Saikia, D. J., Jeyakumar, S., Mantovani, F., et al. 2003, *PASA*, 20, 50
- Sanghera, H. S., Saikia, D. J., Luedke, E., et al. 1995, *A&A*, 295, 629
- Scheuer, P. A. G. 1982, in *Extragalactic Radio Sources*, ed. D. S. Heeschen & C. M. Wade, Vol. 97, 163–165
- Schulz, R., Morganti, R., Nyland, K., et al. 2021, *A&A*, 647, A63
- Scoville, N. Z., Evans, A. S., Thompson, R., et al. 2000, *AJ*, 119, 991
- Shepherd, M. C. 1997, in *Astronomical Society of the Pacific Conference Series*, Vol. 125, *Astronomical Data Analysis Software and Systems VI*, ed. G. Hunt & H. Payne, 77
- Siemiginowska, A., Cheung, C. C., LaMassa, S., et al. 2005, *ApJ*, 632, 110
- Snellen, I. A. G., Schilizzi, R. T., Miley, G. K., et al. 2000, *MNRAS*, 319, 445
- Sobolewska, M., Siemiginowska, A., Guainazzi, M., et al. 2019, *ApJ*, 884, 166
- Sobolewska, M., Siemiginowska, A., Migliori, G., et al. 2023, *ApJ*, 948, 81
- Sokolovsky, K. V., Kovalev, Y. Y., Pushkarev, A. B., Mimica, P., & Perucho, M. 2011, *A&A*, 535, A24
- Stanghellini, C. 2003, *PASA*, 20, 118
- Stanghellini, C., Dallacasa, D., O’Dea, C. P., et al. 2001, *A&A*, 377, 377
- Stanghellini, C., Dallacasa, D., & Orienti, M. 2009a, *Astronomische Nachrichten*, 330, 223
- Stanghellini, C., Dallacasa, D., Venturi, T., An, T., & Hong, X. Y. 2009b, *Astronomische Nachrichten*, 330, 153
- Stanghellini, C., O’Dea, C. P., Baum, S. A., et al. 1997, *A&A*, 325, 943
- Stanghellini, C., O’Dea, C. P., Baum, S. A., & Laurikainen, E. 1993, *ApJS*, 88, 1
- Stanghellini, C., O’Dea, C. P., Dallacasa, D., et al. 1998, *A&AS*, 131, 303
- Stanghellini, C., O’Dea, C. P., Dallacasa, D., et al. 2005, *A&A*, 443, 891
- Sullivan, A. G., Blandford, R. D., Begelman, M. C., Birkinshaw, M., & Readhead, A. C. S. 2024, *MNRAS*, 528, 6302
- Taylor, G. B., Marr, J. M., Pearson, T. J., & Readhead, A. C. S. 2000, *ApJ*, 541, 112
- Taylor, G. B., Readhead, A. C. S., & Pearson, T. J. 1996, *ApJ*, 463, 95
- Tingay, S. J., Macquart, J. P., Collier, J. D., et al. 2015, *AJ*, 149, 74
- Torniainen, I., Tornikoski, M., Teräsanta, H., Aller, M. F., & Aller, H. D. 2005, *A&A*, 435, 839
- Tremblay, S. E., Taylor, G. B., Helmboldt, J. F., Fassnacht, C. D., & Pearson, T. J. 2008, *ApJ*, 684, 153
- Tremblay, S. E., Taylor, G. B., Ortiz, A. A., et al. 2016, *MNRAS*, 459, 820
- van Breugel, W., Miley, G., & Heckman, T. 1984, *AJ*, 89, 5
- Vink, J., Snellen, I., Mack, K.-H., & Schilizzi, R. 2006, *MNRAS*, 367, 928
- Wilkinson, P. N., Polatidis, A. G., Readhead, A. C. S., Xu, W., & Pearson, T. J. 1994, *ApJ*, 432, L87
- Wu, F., An, T., Baan, W. A., et al. 2013, *A&A*, 550, A113
- Xiang, L., Stanghellini, C., Dallacasa, D., & Haiyan, Z. 2002, *A&A*, 385, 768
- Yang, X., Liu, X., Yang, J., et al. 2017, *MNRAS*, 471, 1873
- Yu, Q. 2002, *MNRAS*, 331, 935

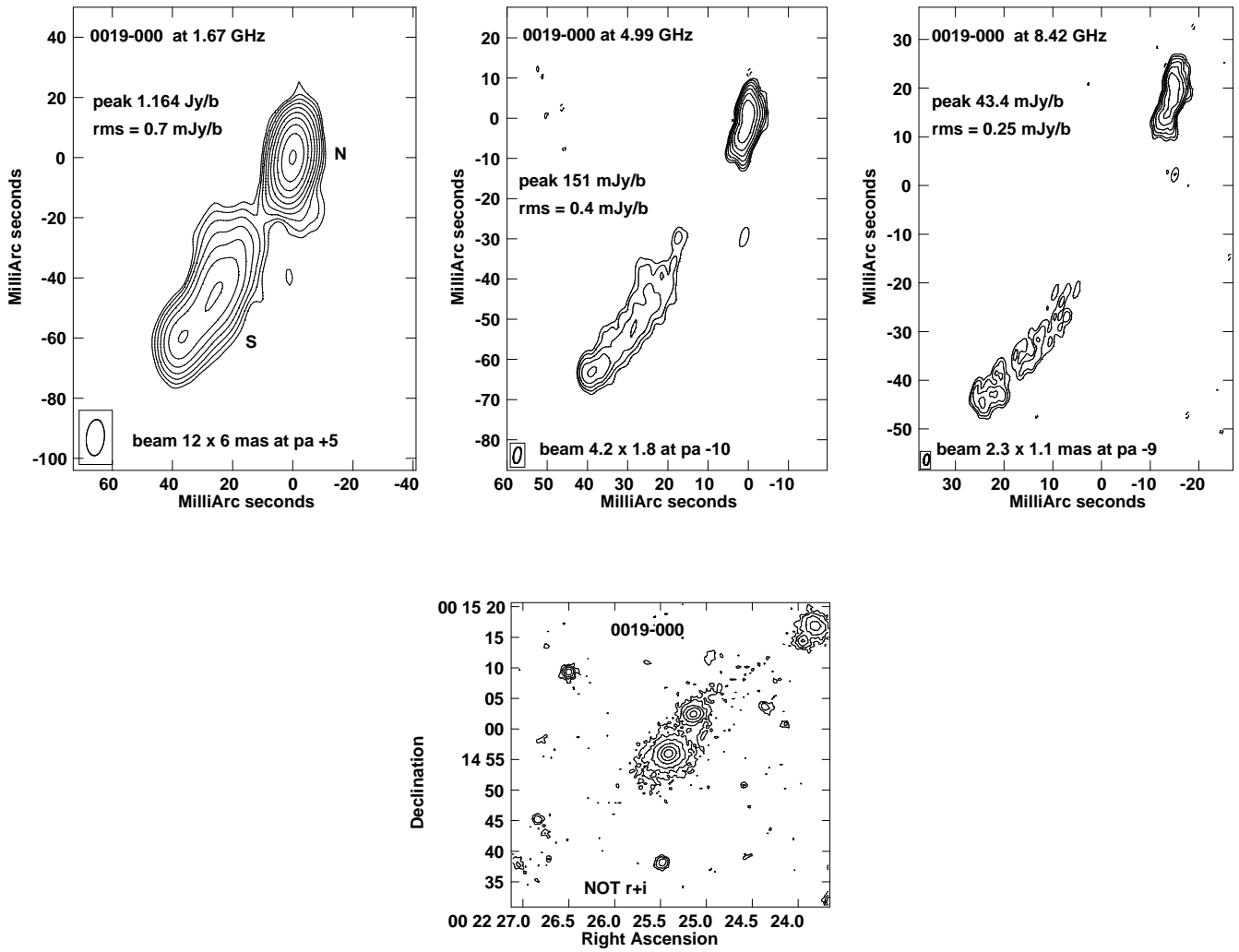


Fig. 4. 0019-000 - here and in the following images, first contour is 3 times the rms on the image, and contour levels progress geometrically (-3,3,6,12,24,48 etc); optical host from NOT r+i band. Nordic Optical Telescope (NOT) observations are described in Stanghellini et al. (1993)

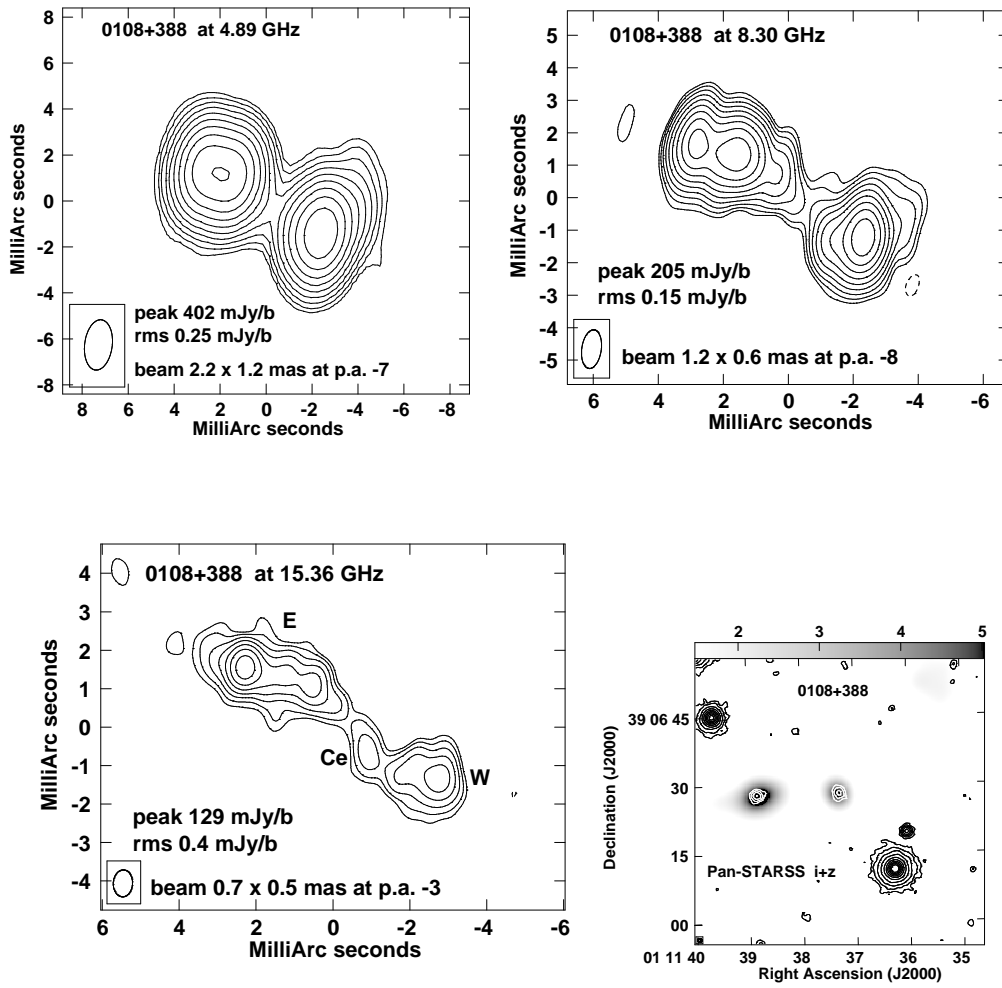


Fig. 5. 0108+388 - VLBA images at 4.89, 8.30, and 15.36 GHz. Optical image from Pan-STARSS stacking of i and z bands superimposed to radio emission in grey scale (VLA:AS637 at 1.36 GHz)

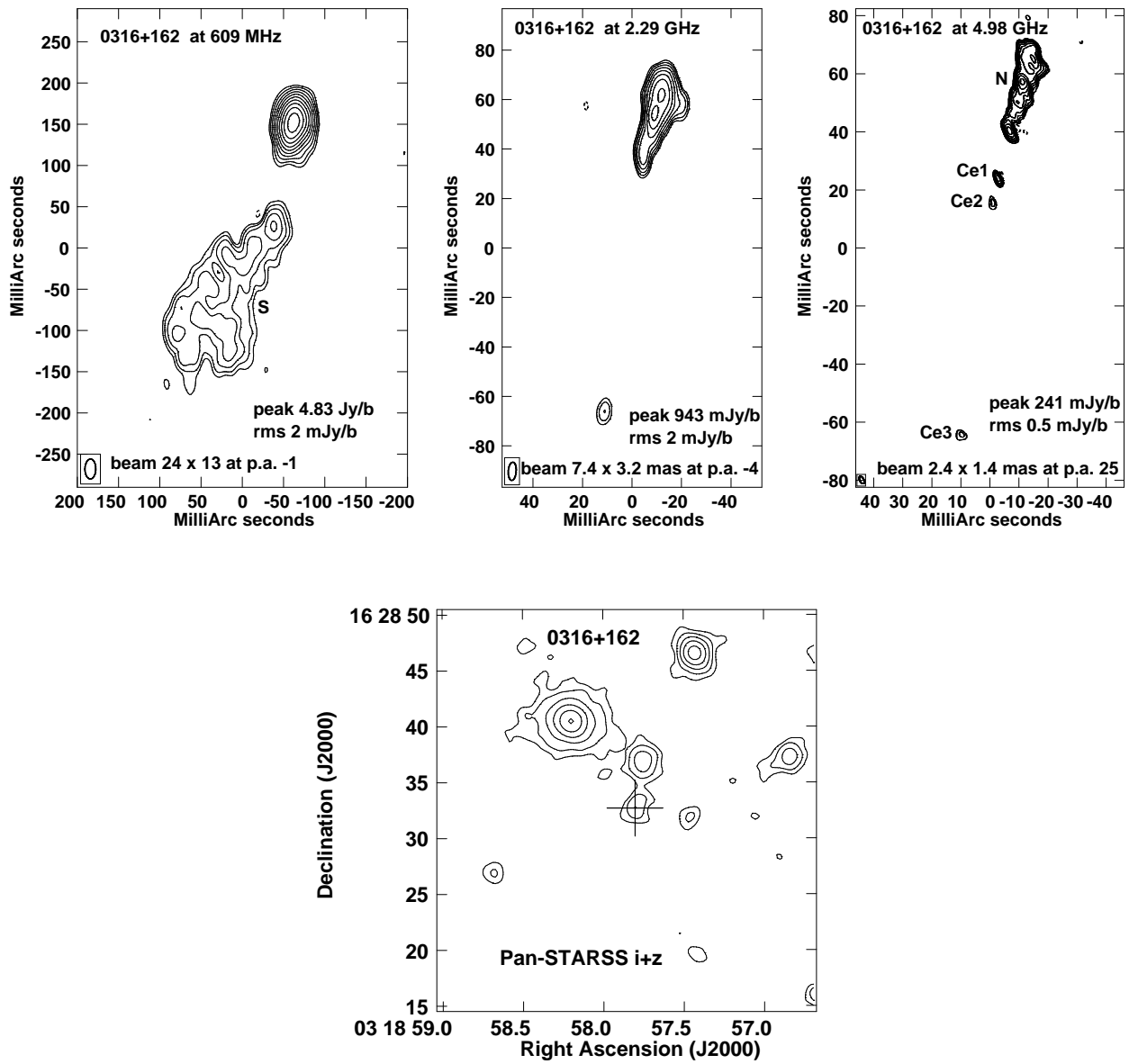


Fig. 6. 0316+162 - VLBA images at 0.609, 2.29, and 4.98 GHz. Optical image from Pan-STARSS stacking of i and z bands; a cross marks the radio position.

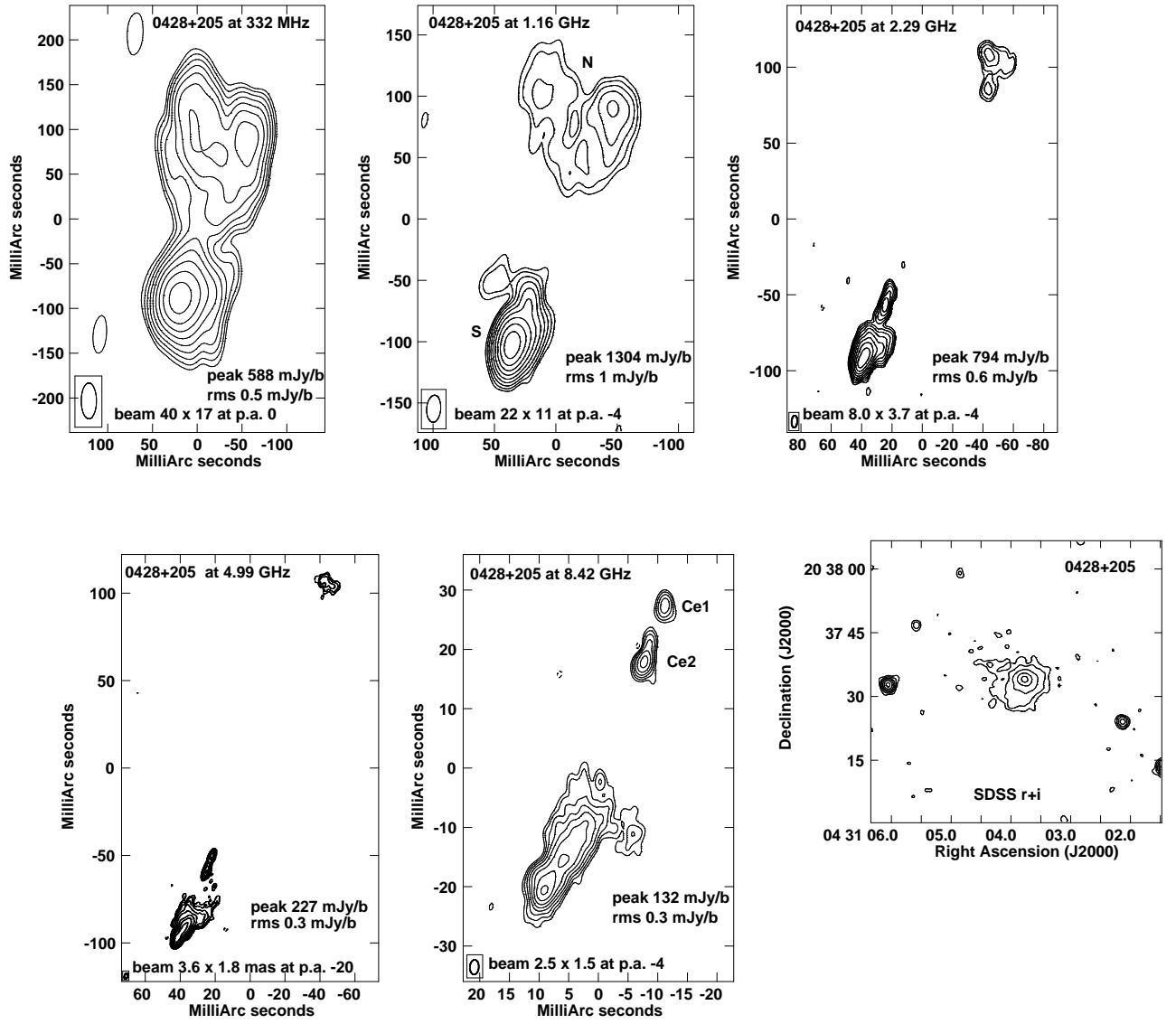


Fig. 7. 0428+205 at 0.333, 1.16, 2.29, 4.99, and 8.42 GHz - Optical image from Sloan Digital Sky Survey (SDSS) stacking of r and i bands.

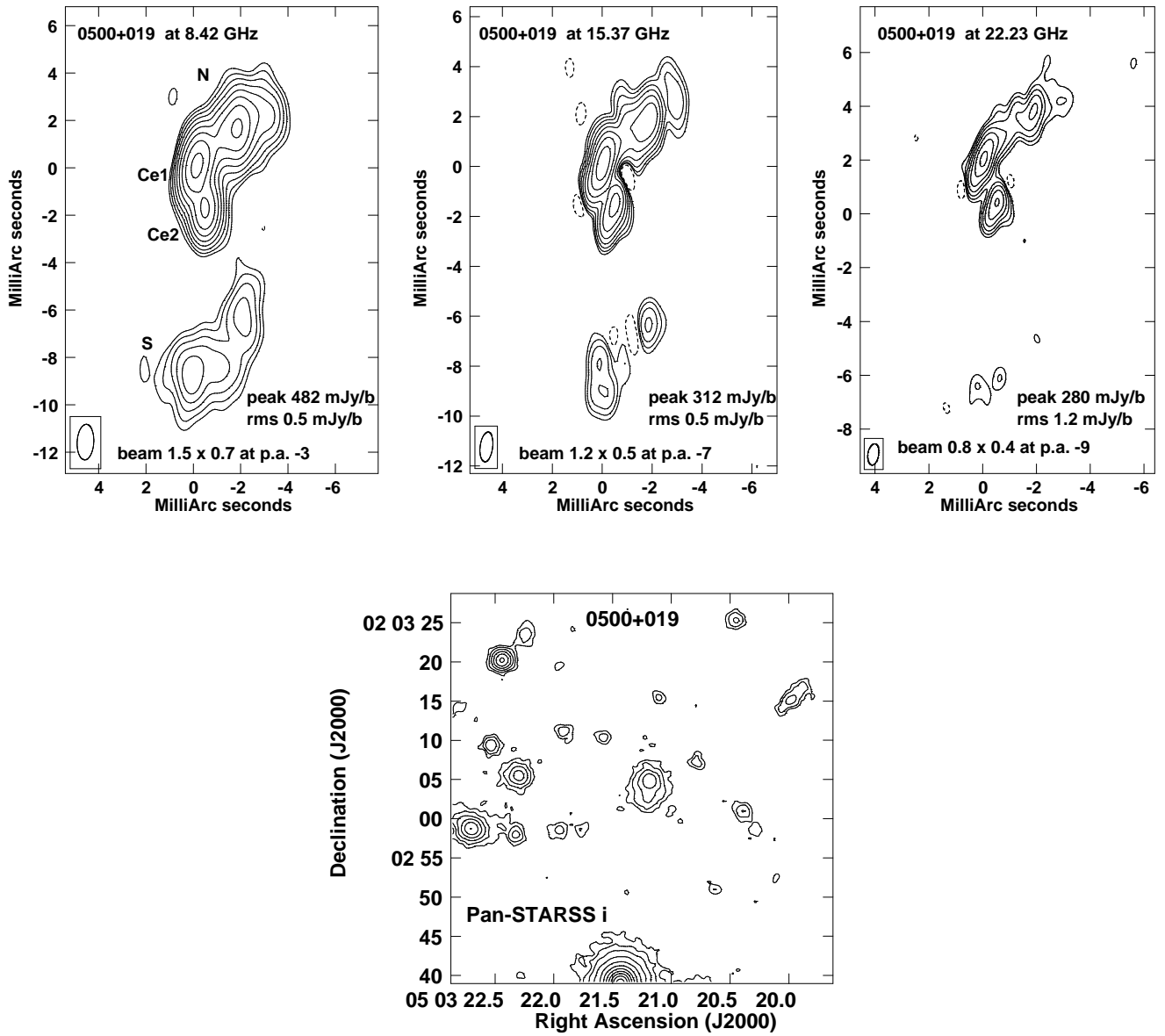


Fig. 8. 0500+019 at 8.42, 15.37 and 22.23 GHz; optical image in i band from Pan-STARRS

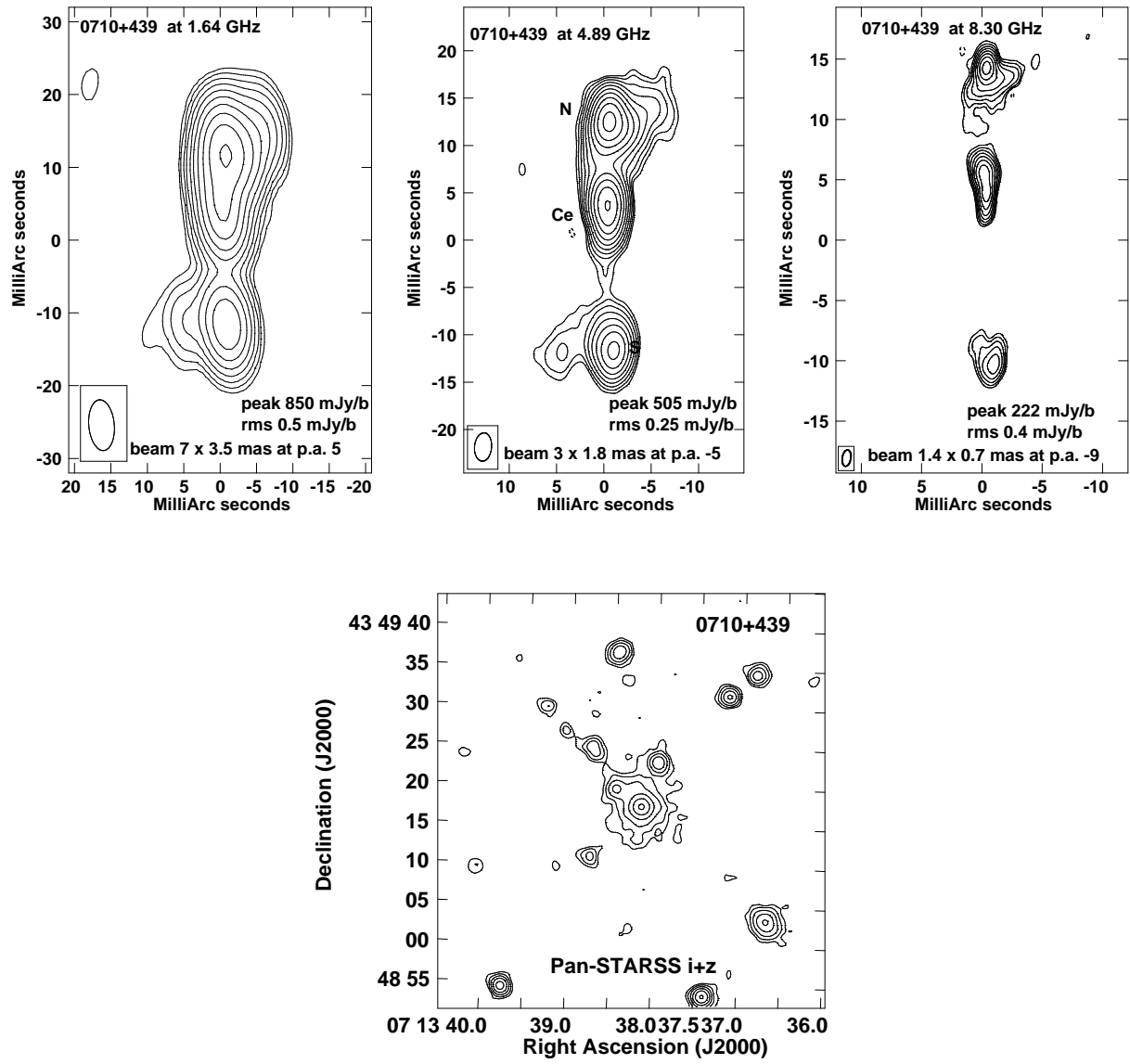


Fig. 9. 0710+439 - VLBA images at 1.64, 4.89, and 8.30 GHz. Optical image from Pan-STARSS

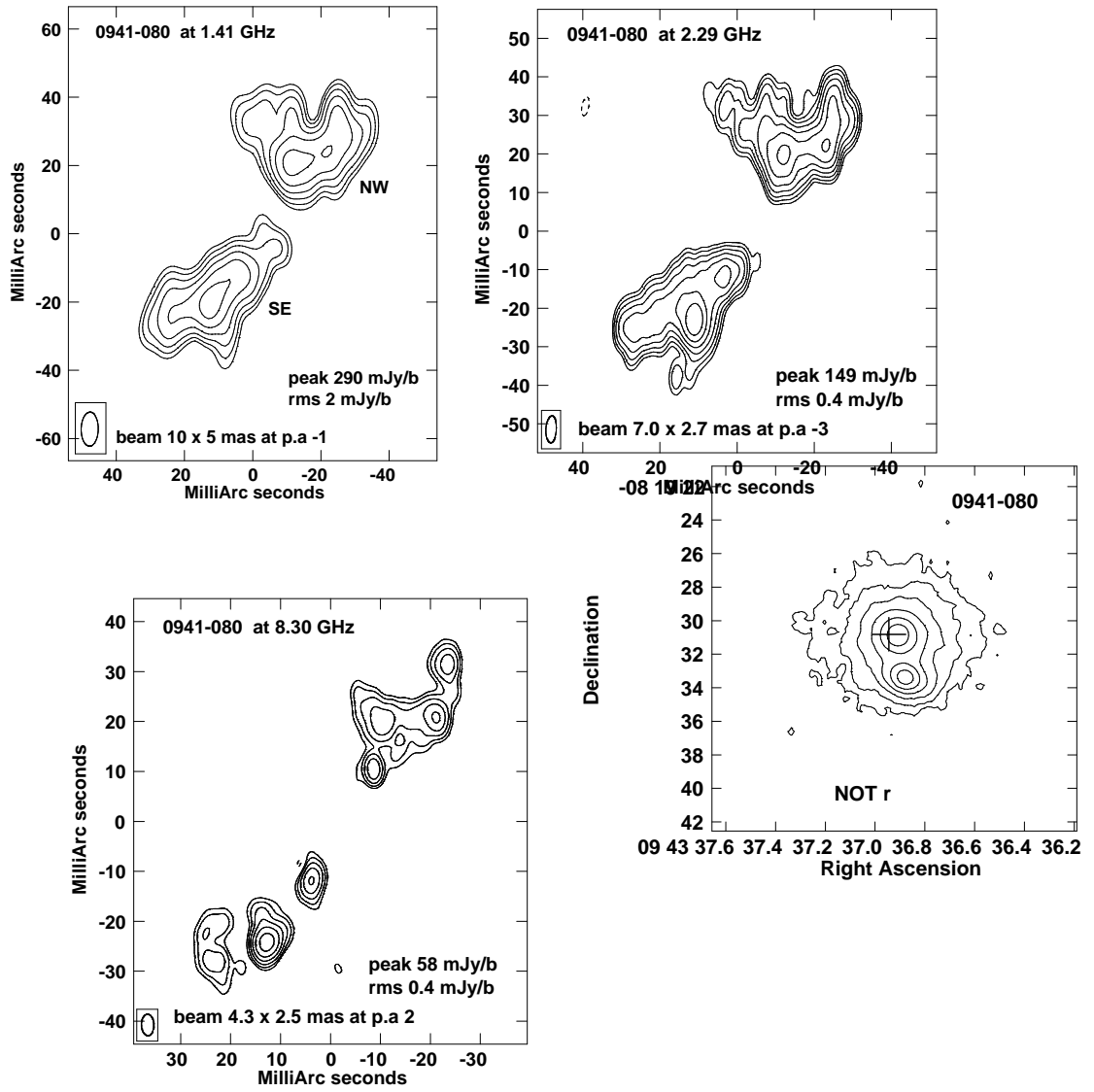


Fig. 10. 0941 at 1.41, 2.29 and 8.30 GHz; optical host from NOT r band; a cross marks the radio position.

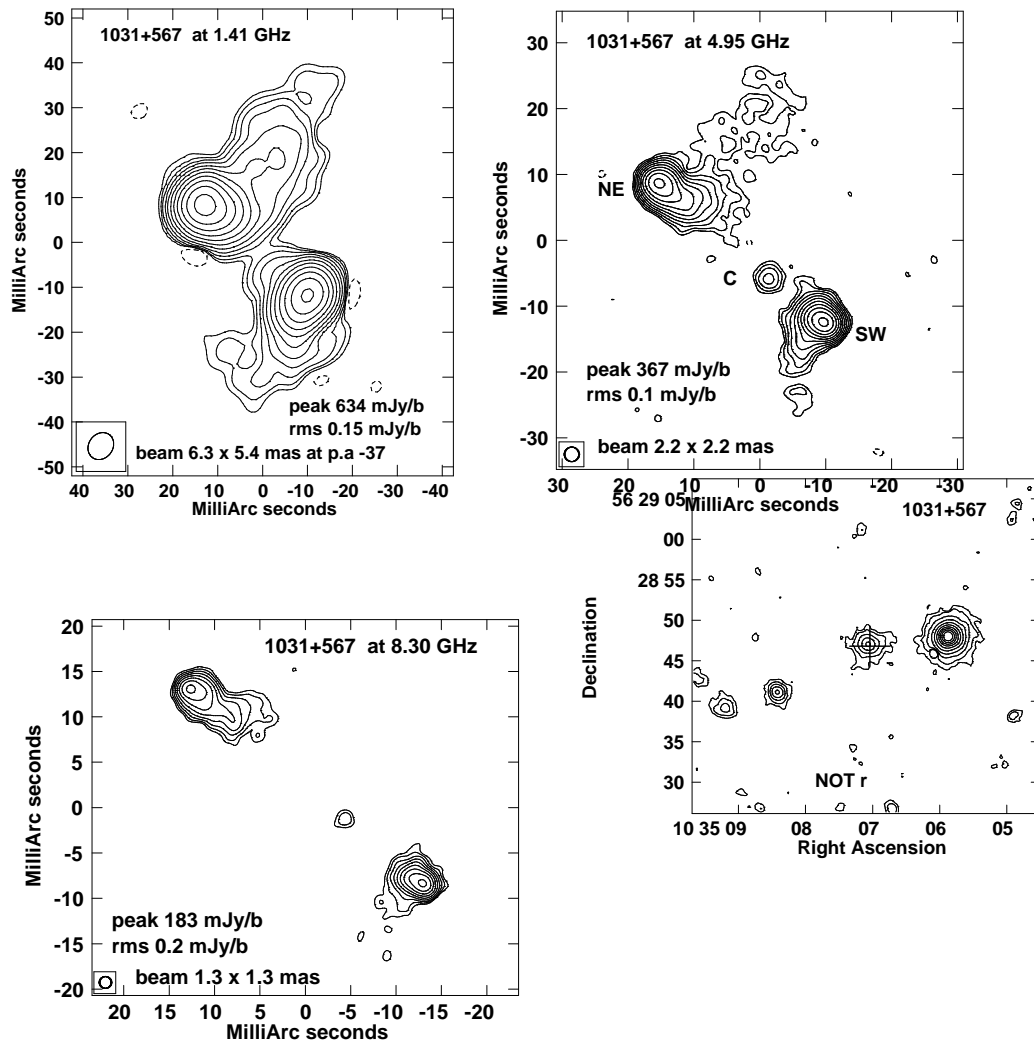


Fig. 11. 1031+567 - VLBA images at 1.41, 4.95, and 8.30 GHz. Optical image from NOT, r band; a cross marks the radio position.

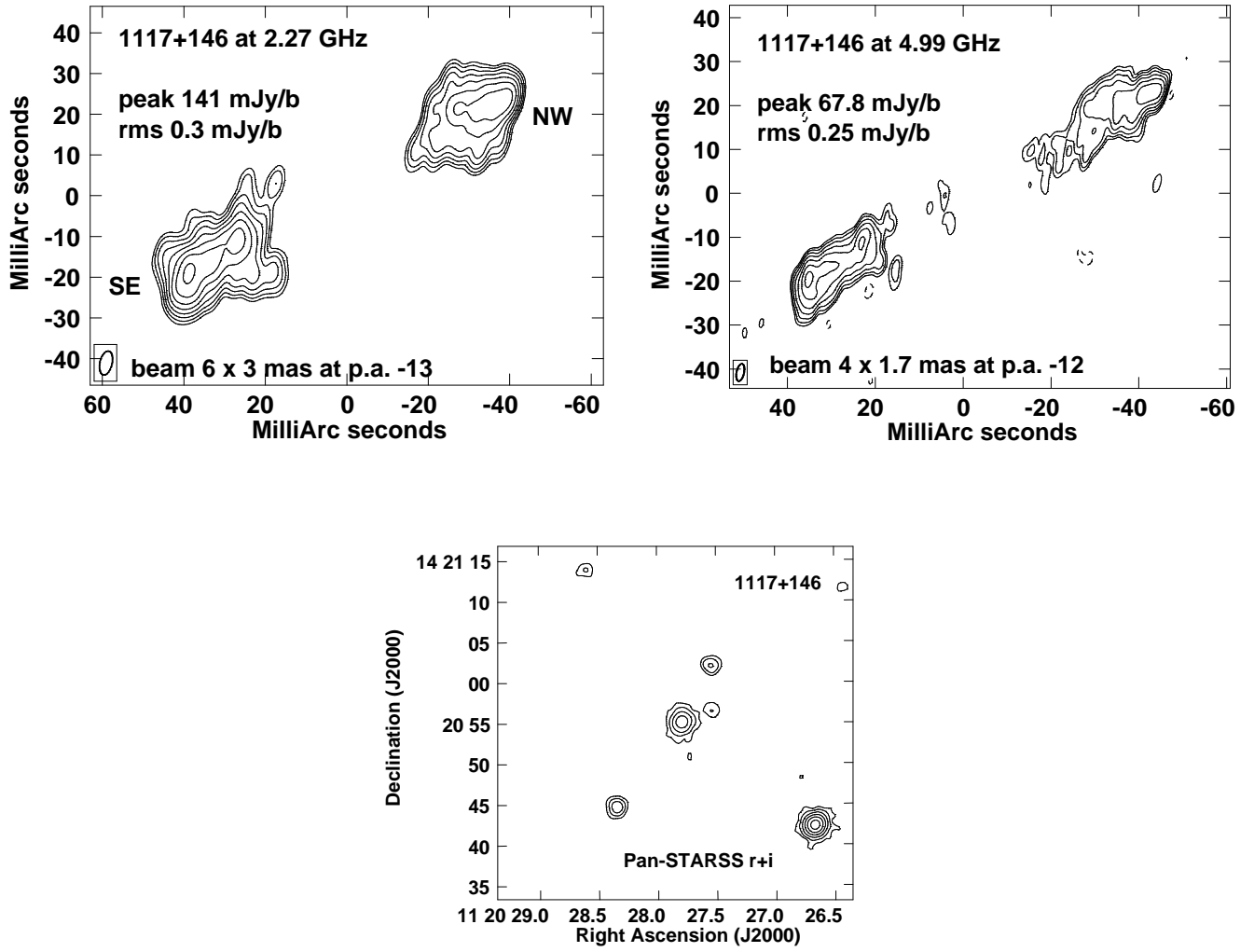


Fig. 12. 1117+146 at 2.27 and 4.99 GHz - Optical image from Pan-STARRS, stacking of r and i bands.

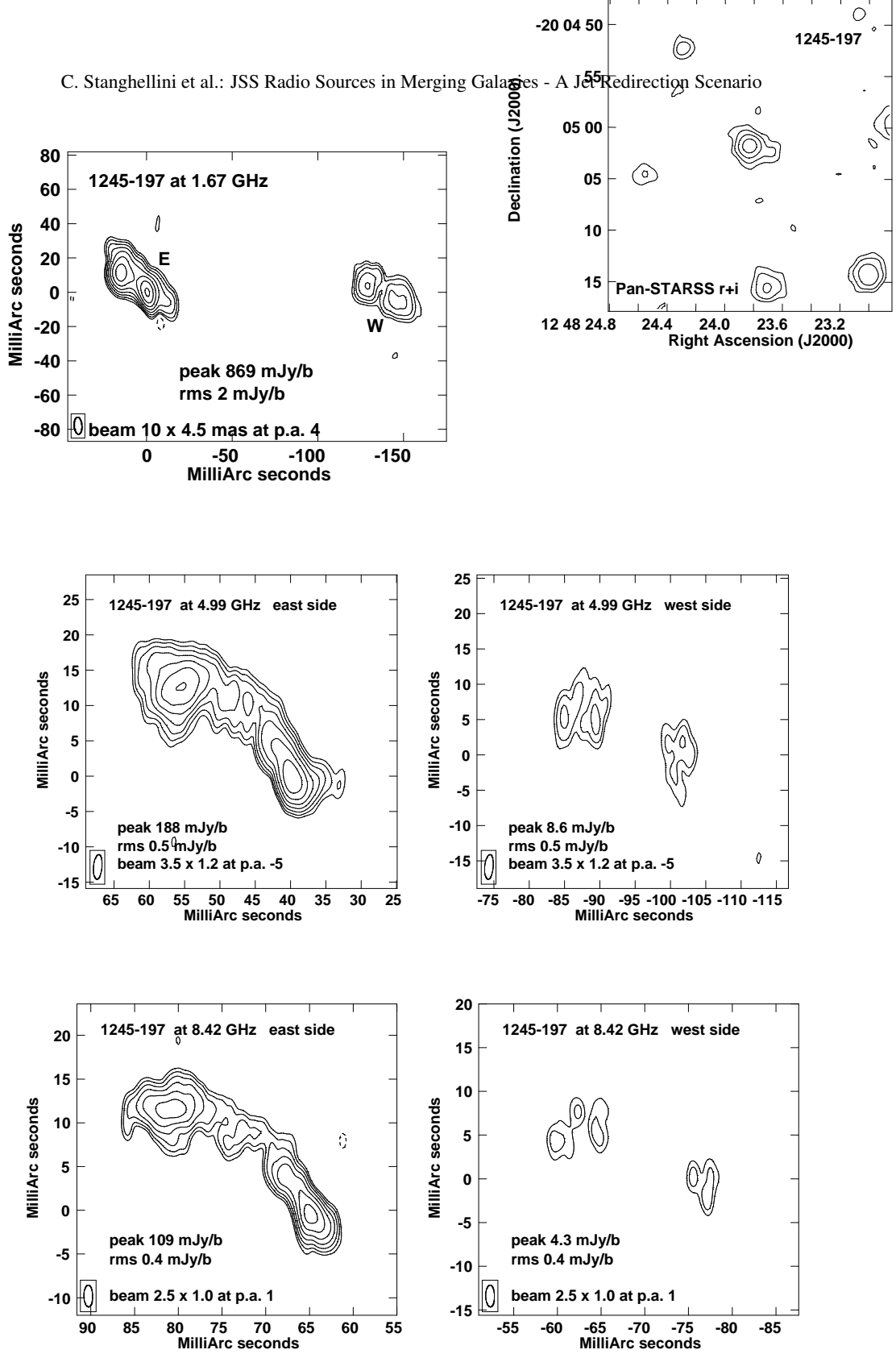


Fig. 13. 1245-196 at 1.67 GHz, 4.99, 8.42 GHz. Optical image from Pan-STARRS, stacking of r and i bands

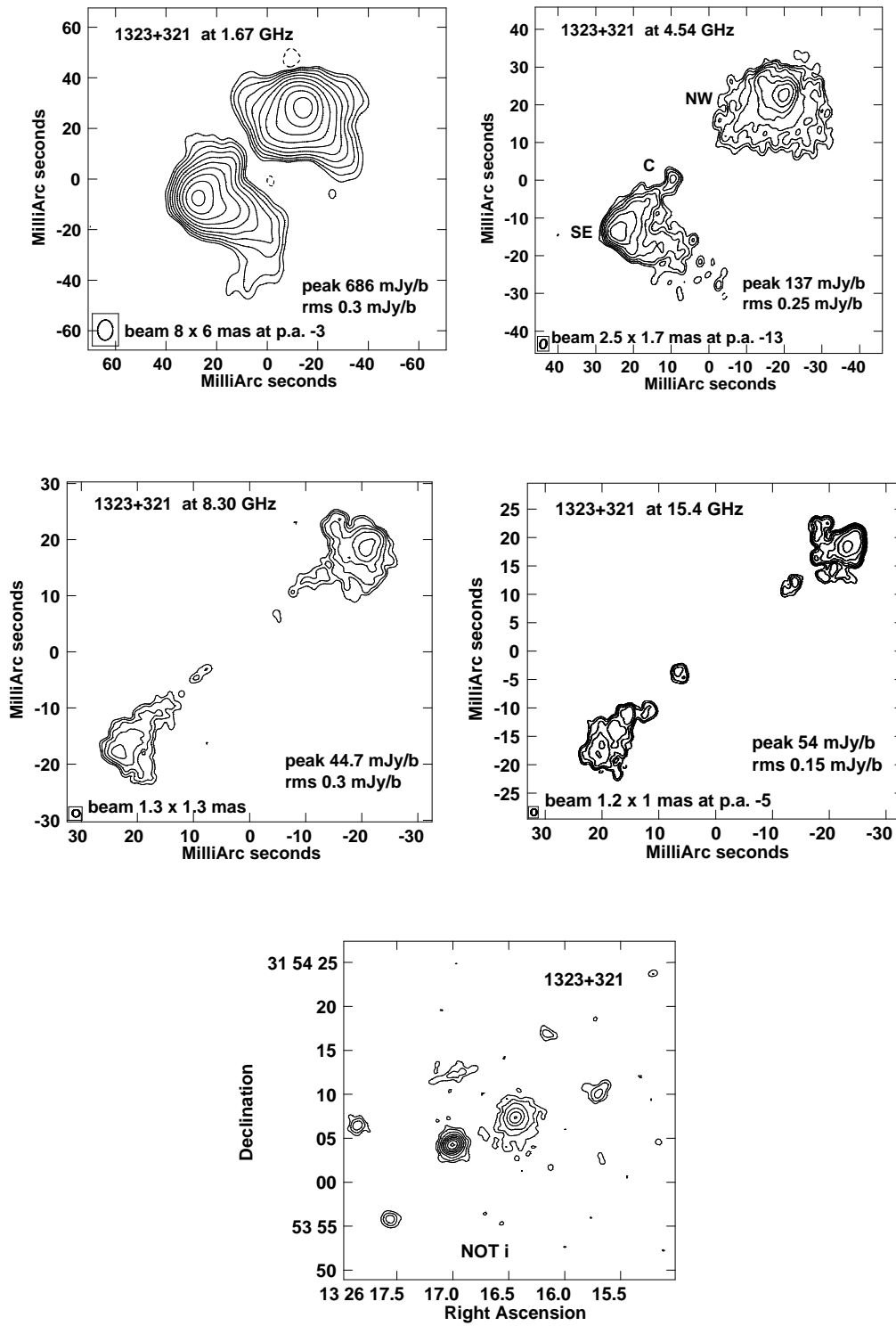


Fig. 14. 1323+321 - VLBA image at 1.67, 4.54, 8.30, and 15.4 GHz. Optical image from NOT, i band.

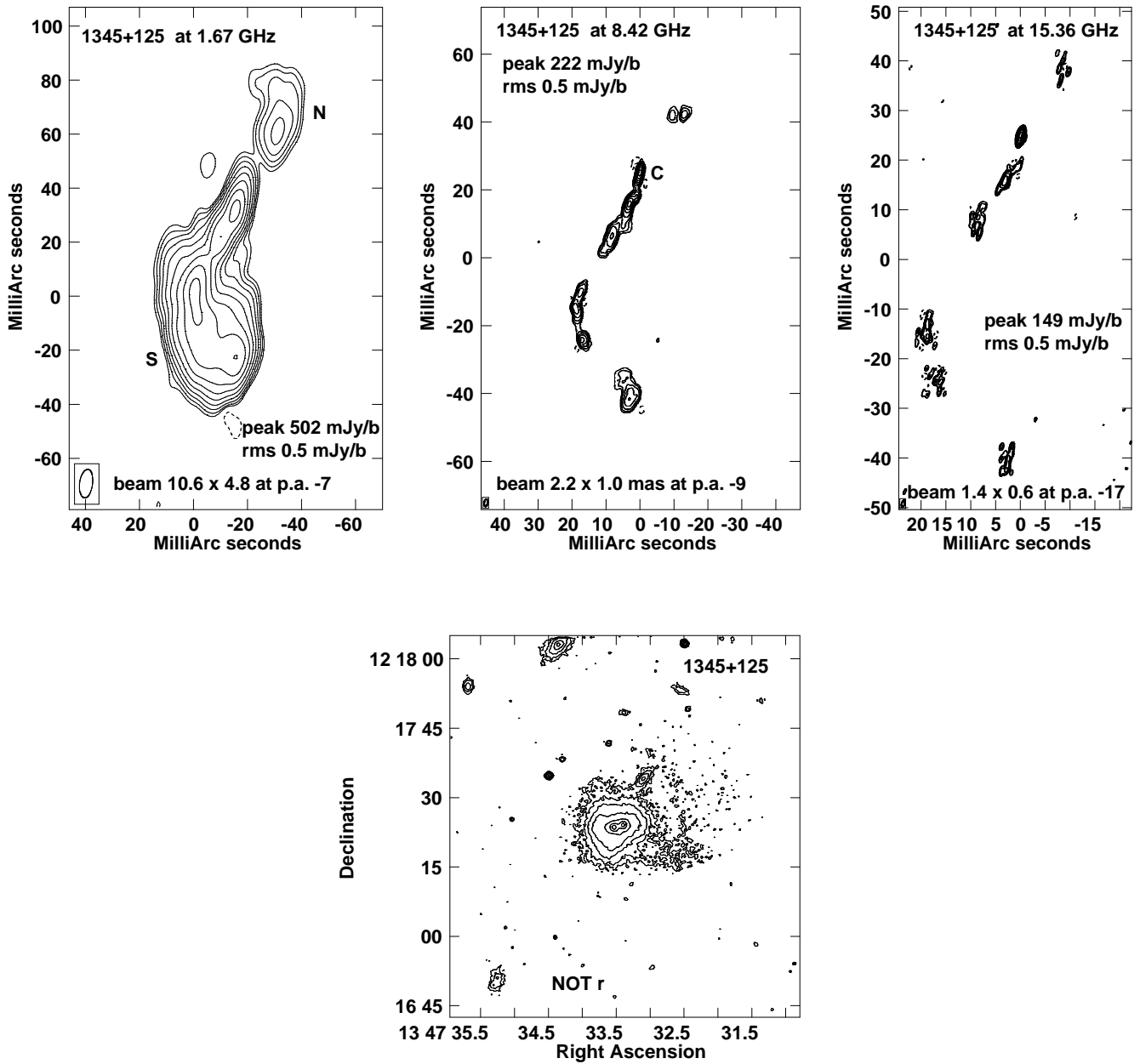


Fig. 15. 1345+125 at 1.67, 8.42, 15.36 GHz. Optical image from NOT, r band

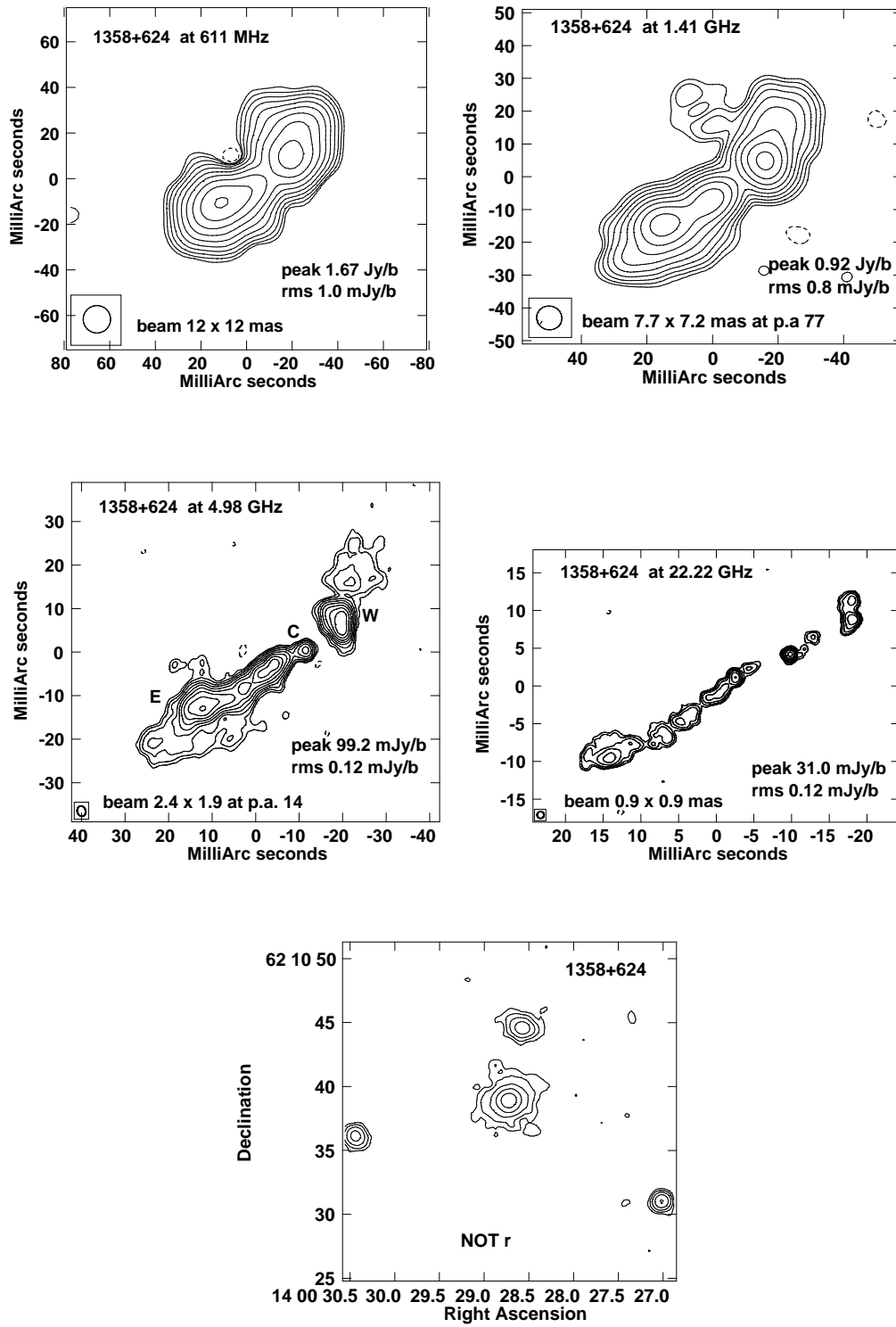


Fig. 16. 1358+624 - VLBA images at 0.611, 1.41, 4.98, and 22.22 GHz. Optical image from NOT, r band.

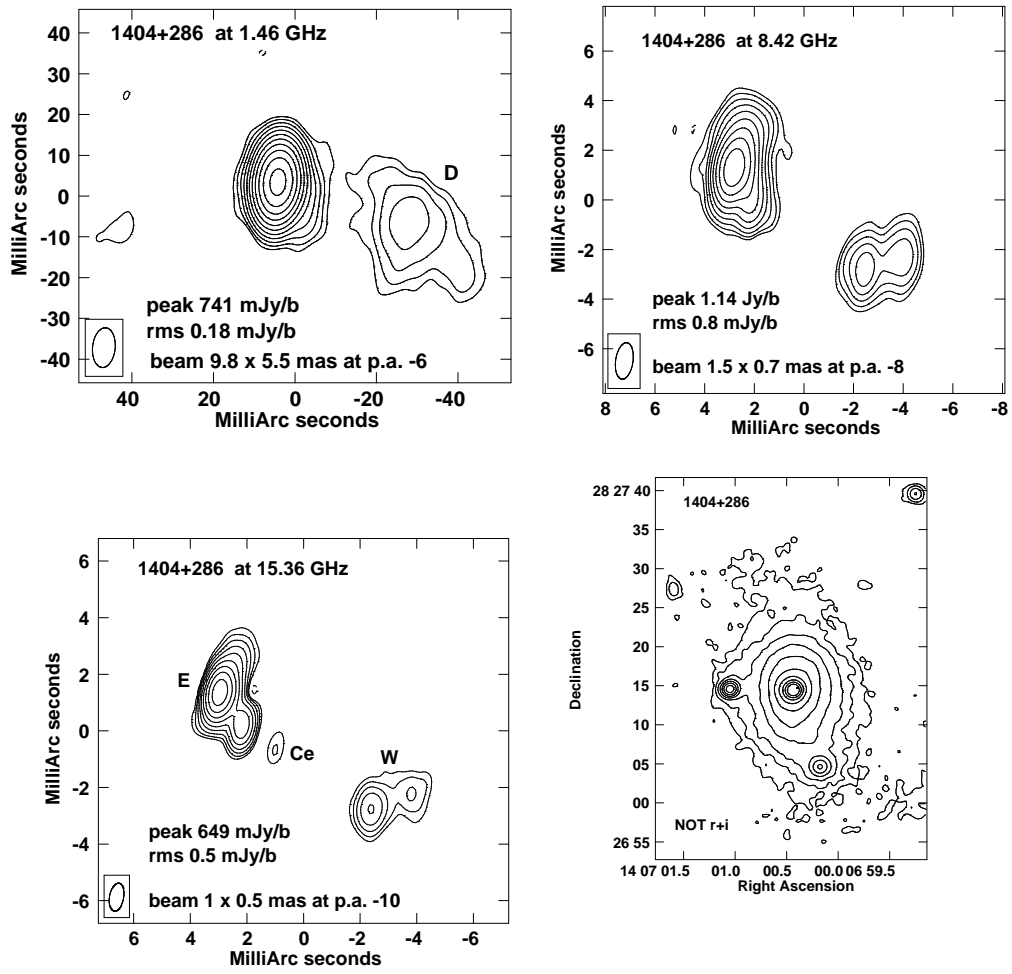


Fig. 17. 1404+286 at 1.67, 8.42 and 15.36 GHz; optical image from NOT, stacking of r and i bands.

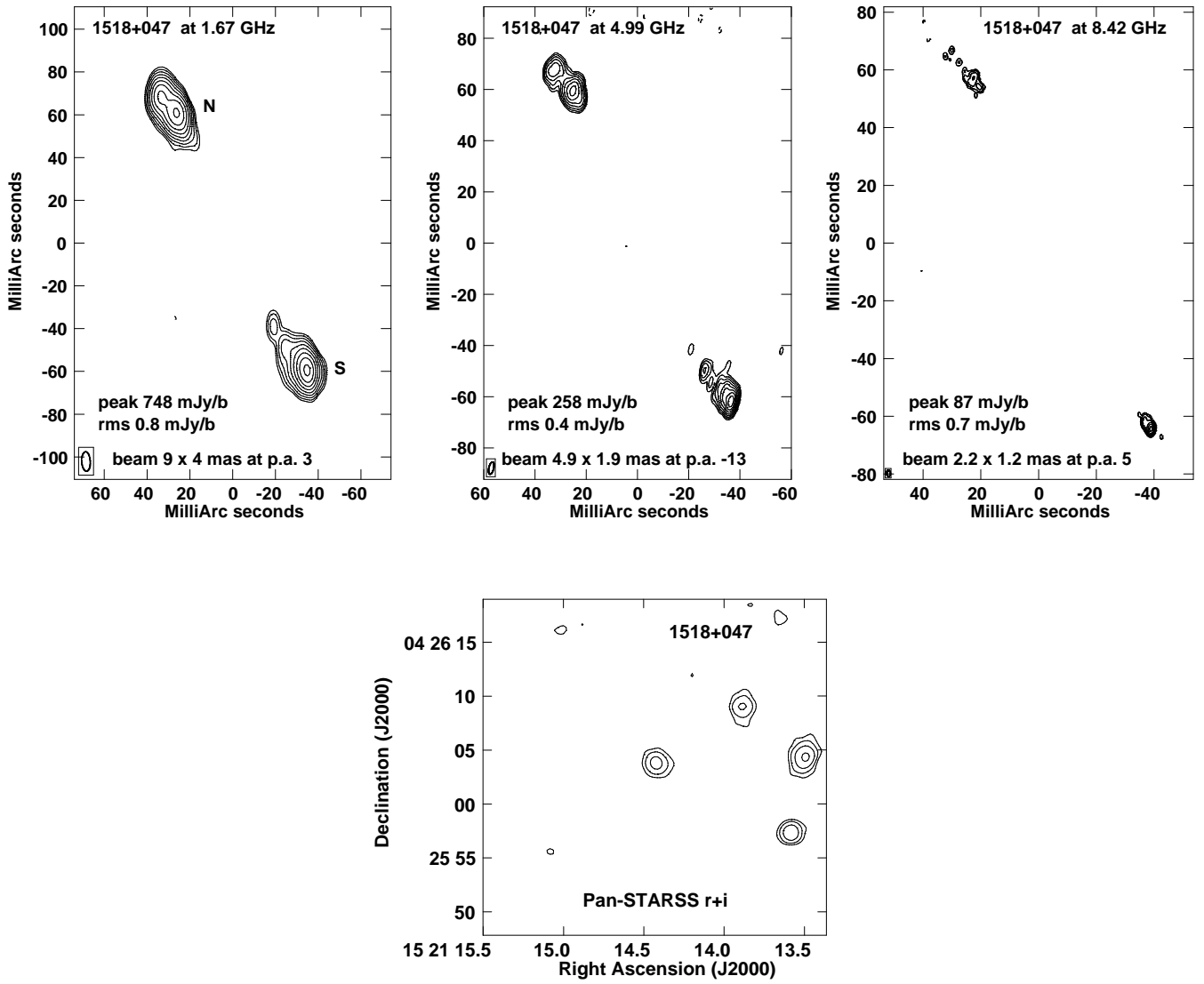


Fig. 18. 1518+047 - VLBA images 1.67, 4.99, and 8.42 GHz. Optical image from Pan-STARRS, stacking of r and i bands.

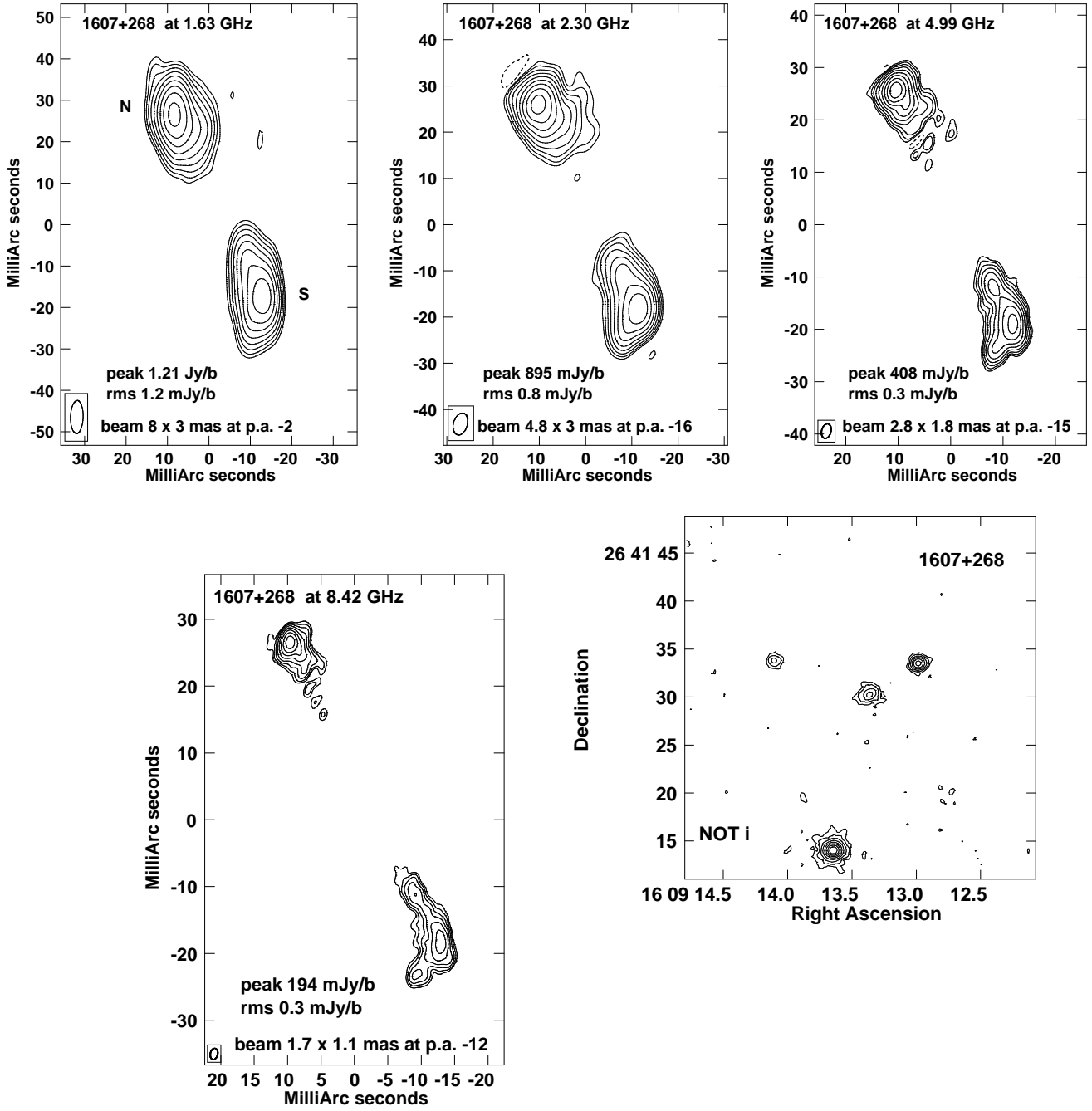


Fig. 19. 1607+268 - VLBA images at 1.63, 2.30, 4.99, and 8.42 GHz. Optical image from NOT, i band.

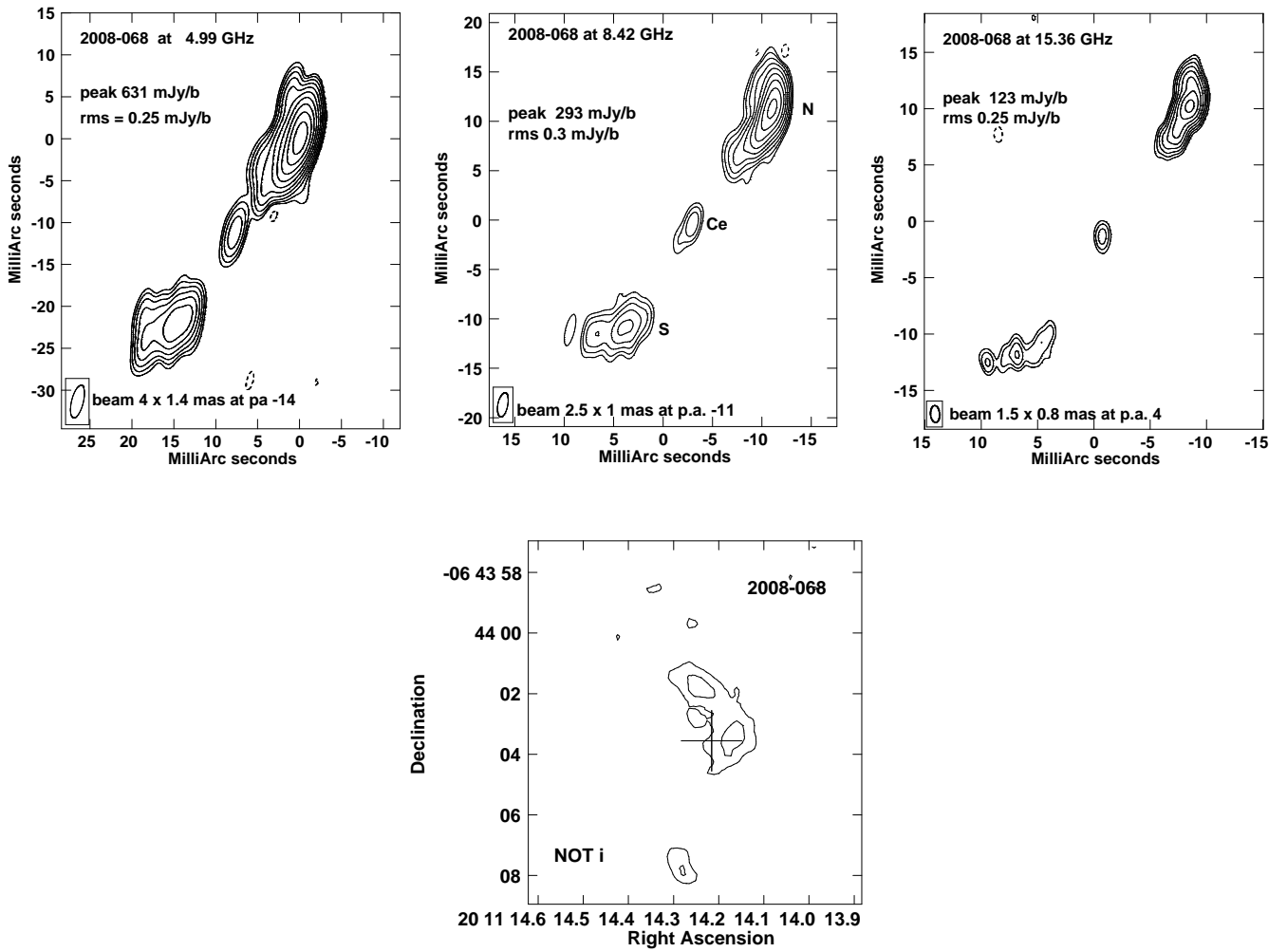


Fig. 20. 2008-068 - VLBA images at 4.99, 8.42, and 15.36 GHz; optical image from NOT, i band.

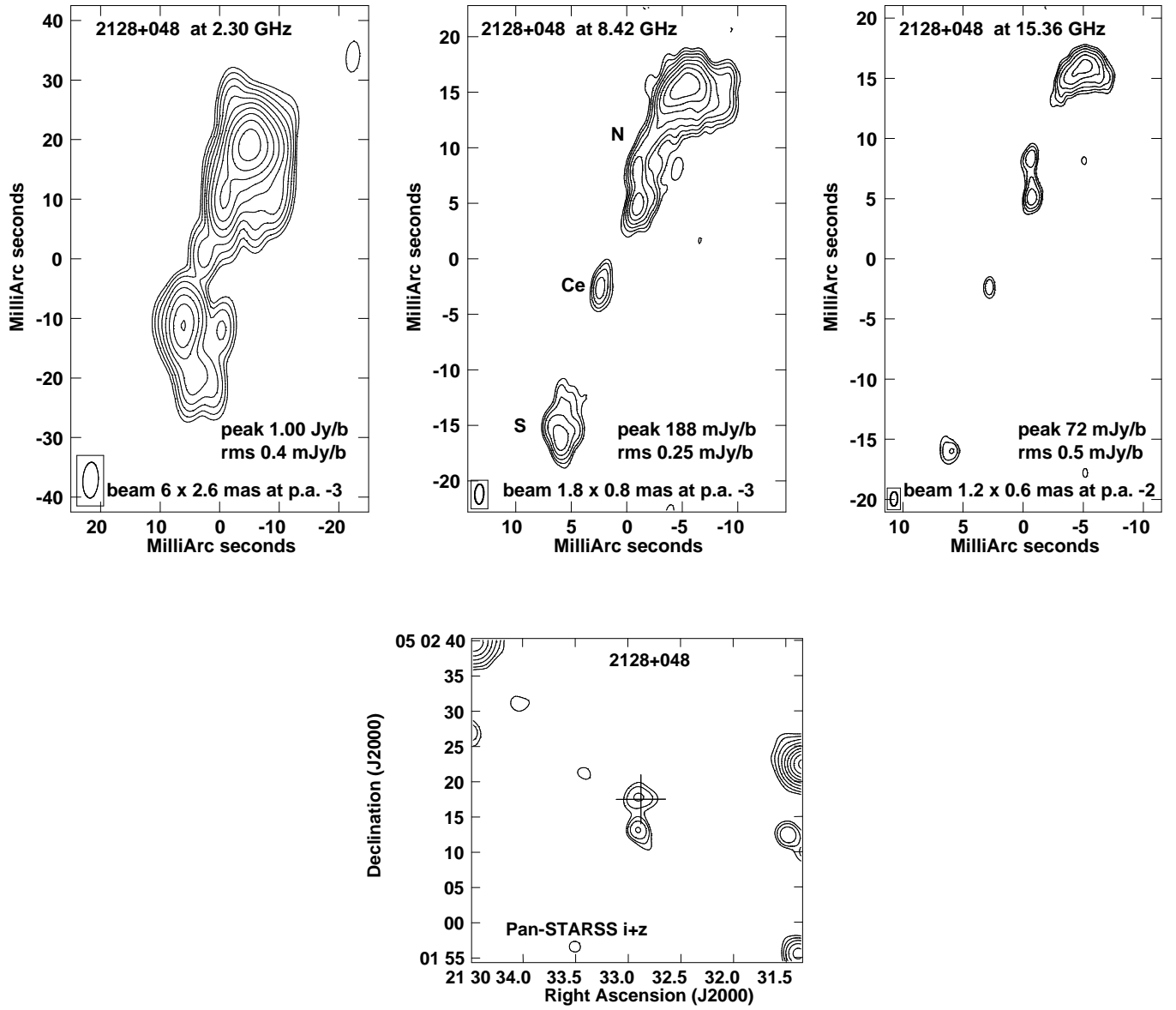


Fig. 21. 2128+048 - VLBA images at 2.30, 8.42, and 15.36 GHz. Optical image from Pan-STARSS stacking of i and z bands; a cross marks the radio position.

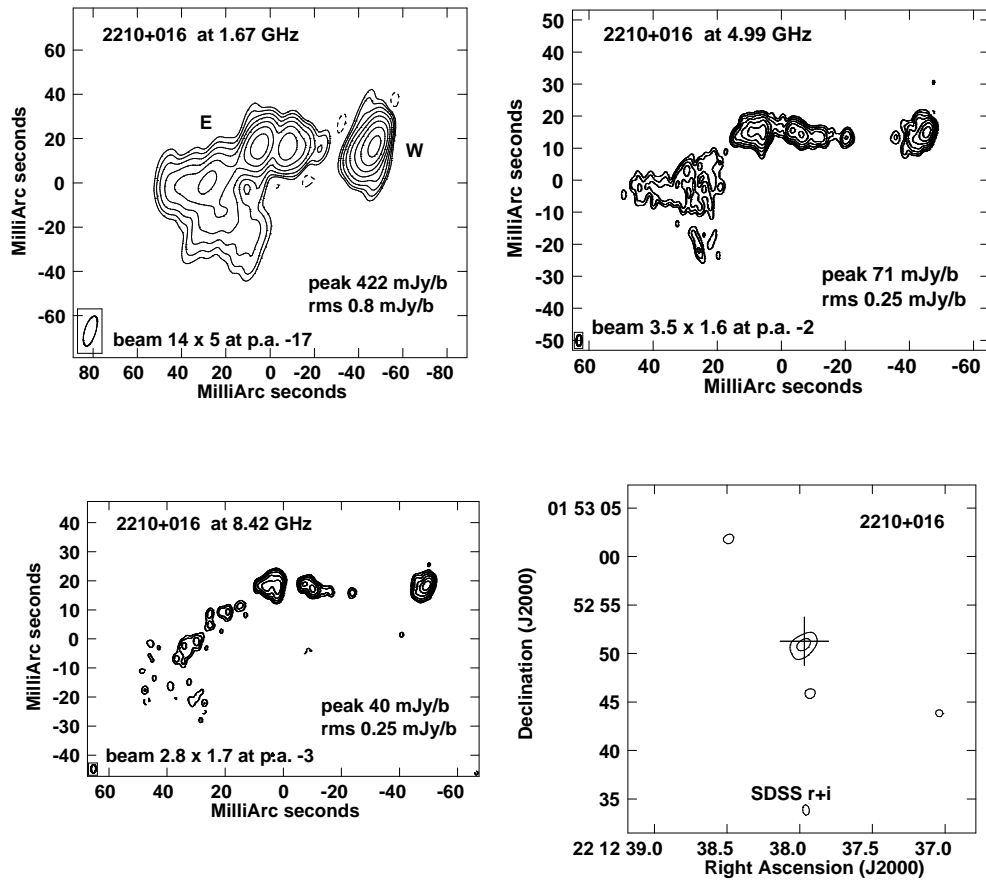


Fig. 22. 2210+016 - VLBA images at 1.67, 4.99, and 8.42 GHz. Optical image from SDSS, stacking of r and i bands.

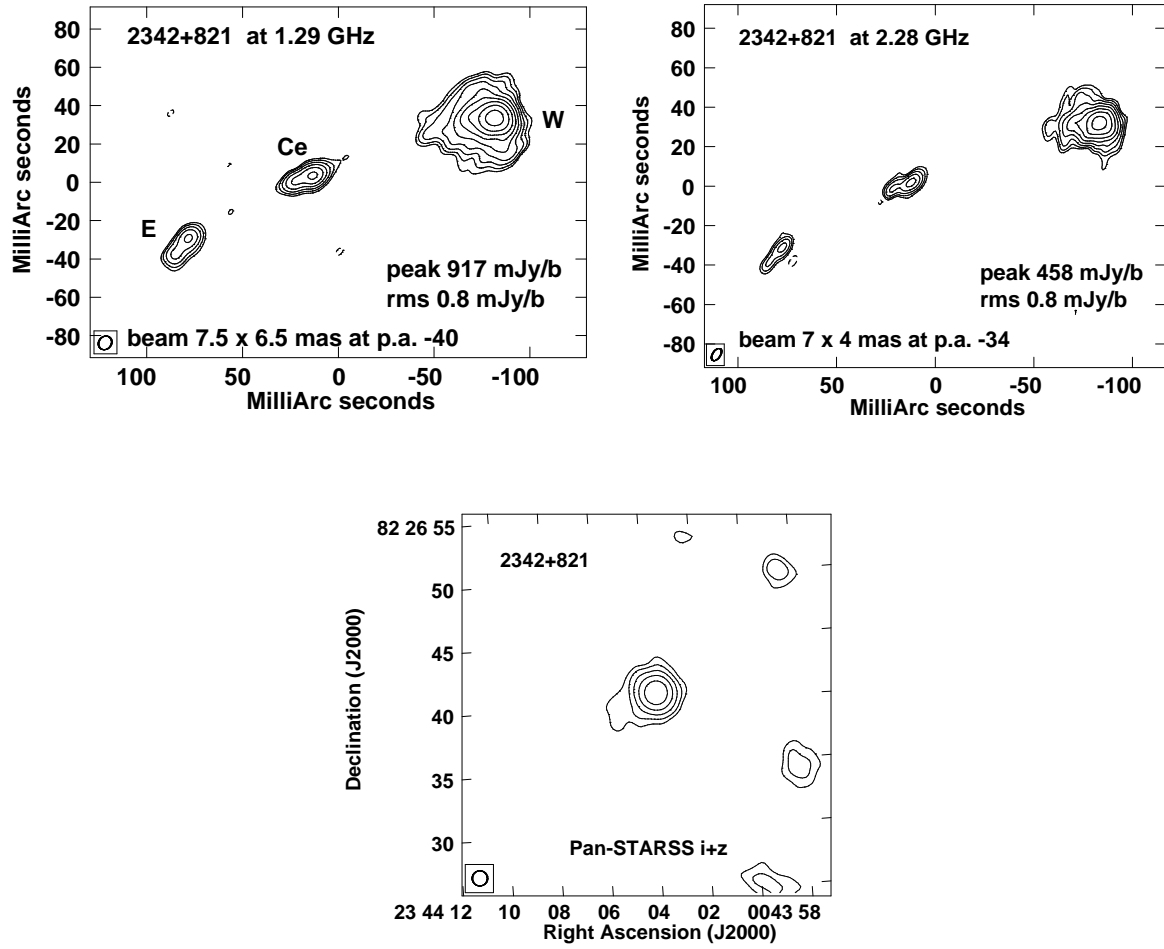


Fig. 23. 2342+821 - VLBA image at 1.29 and 2.28 GHz. Optical image from Pan-STARRS, stacking of i and z bands.

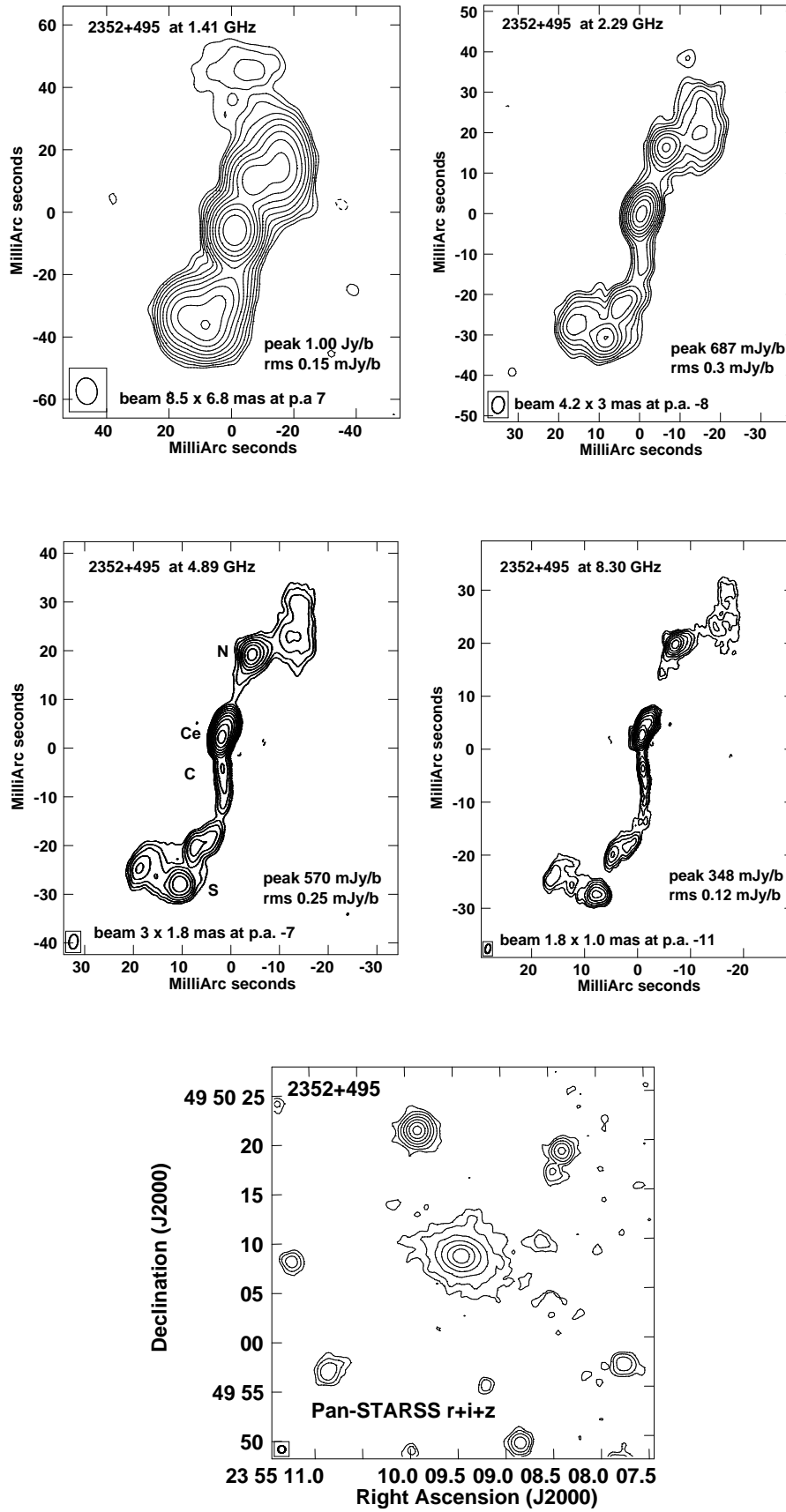


Fig. 24. 2352+495 - VLBA images at 1.41, 2.29, 4.89, and 8.30 GHz. Optical image from Pan-STARRS, stacking of r, i and z bands.